universität wien

DIPLOMARBEIT

Titel der Diplomarbeit

''Efficiency and uniformity of a SiPM array combined with a light concentrator''

Verfasserin

Mariana Rihl

angestrebter akademischer Grad

Magistra rerum naturalium (Mag.rer.nat.)

DIPLOMA THESIS

Title of the diploma thesis

"Efficiency and uniformity of a SiPM array combined with a light concentrator"

Author

Mariana Rihl

Aspired academic degree

Magistra rerum naturalium (Mag.rer.nat.)

Vienna, November 2012

Study code: A 411
Branch of study: Physics
Advisor: Prof. Dr. Eberhard Widmann

Dedicated to my parents

Abstract

Silicon photomultipliers (SiPMs) are solid-state photon detectors based on the principle of single photon avalanche diodes (APDs). These APDs of a SiPM matrix are operated in Geiger mode and provide a good photon detection efficiency. SiPMs are compact in size, have a low power consumption and are insensitive to magnetic fields. Furthermore their use is cost efficient, which makes them, in addition to the previously mentioned characteristics, suitable for many research fields, such as particle physics, astrophysics, nuclear physics or medical imaging.

One application of SiPMs is the detection of Cherenkov light and with multiple SiPMs arranged in an array, a spatial resolution is possible. A position sensitive Cherenkov light detection module was built at the Stefan Meyer Institute. It consists of 64 SiPMs, which are arranged in a 8×8 matrix. On top of the array a so-called "light concentrator" is mounted. This light concentrator increases the sensitive area of the sensors, thus reducing the costs of the detector. In this work, the detector prototype was tested in terms of light collection efficiency and uniformity; in order to prove that the concept of a light concentrator is useful in experiments with Cherenkov light.

Zusammenfassung

Silicium Photomultiplier (SiPM) sind Halbleiter-Photodetektoren, die auf dem Prinzip von Einzelphotonen Avalanchedioden (APDs) basieren. Die vielen APDs, die in einem SiPM matrixförmig angeordnet sind, werden im Geigermodus betrieben und haben eine gute Effizienz für Photonendetektion. SiPMs sind sehr kompakt, brauchen im Betrieb wenig Energie und funktionieren störungsfrei in Magnetfeldern. Zusätzlich zu diesen Eigenschaften sind sie günstig in der Anschaffung, was sie für viele Forschungsfelder, wie z.B. Teilchen- oder Kernphysik, Astrophysik oder medizinische bildgebende Verfahren nützlich macht.

Eine Anwendung von SiPMs ist die Messung von Cherenkov-Strahlung, wobei bei einer Anordnung von mehreren SiPMs in einer Matrix auch eine Positionsauflösung möglich ist. Ein positionsauflösender Cherenkov-Licht Detektor wurde am Stefan-Meyer-Institut konzipiert und gebaut. Der Detektor besteht aus 64 SiPMs, die in einer quadratischen 8×8 Matrix angeordnet sind. Auf dieser Anordnung wurde ein sogenannter "light concentrator" fixiert, der die sensitive Fläche der Sensoren vergrößern, und somit die Kosten des Detektors verringern soll. In dieser Diplomarbeit wurde der Detektorprototyp bezüglich Uniformität und Effizienz der Lichtsammlung überprüft. Die Ergebnisse zeigen, dass sich ein "light concentrator" für Experimente in denen Cherenkov-Licht gemessen wird, als nützlich erweist.

Contents

1. Introduction

Photodetection with photomultiplier tubes (PMTs) plays an important role in particle physics, where the detection of photons is used with scintillation counters for example to detect positrons, muons or to directly detect Cherenkov light [1]. These tubes use the principle of the photoelectric effect, where an incident photon sets an electron free in the photocathode. As the PMT has a voltage applied, the electron gets accelerated in a certain direction to a dynode, where it knocks out several secondary electrons, which again get accelerated towards the next dynode and so on, until the electron cascade reaches the anode where the current can be picked up and provide a signal.

A newer technology to detect photons are silicon photomultipliers (SiPM). These sensors have some advantages over PMTs. SiPMs work at a lower operating voltage ($\leq$ 100 V) than PMTs ($\geq$ kV) while providing about the same gain. Also, SiPMs are more sensitive in the blue-light range than PMTs [2], which makes them suitable for scintillators that emit blue light and for applications that include Cherenkov light. Another large advantage of SiPMs over PMTs is their insensitivity to magnetic fields, which can be explained by the dimensions of the two devices:

If a PMT is placed in a magnetic field, it has an influence on the path of the electron cascade, as it curves the path of the electrons. This influence is far greater for an electron in a PMT than for a SiPM, because the distance between the cathode and the first dynode is much larger than the dimension of a pixel of a SiPM. This means that in a PMT, a magnetic field causes the electrons to deviate from the path they would follow without a magnetic field, so fewer electrons impact at the (next) dynode, which leads to a reduced gain or in the worst case to a cascade breakdown where no signal can be measured at all. Magnetic shielding was used to reduce this problem. SiPMs are insensitive to magnetic fields, so the magnetic fields which are applied in particle physics experiments or in medical imaging have no influence on the signal. This makes the expensive magnetic shielding obsolete, which is another advantage of SiPMs.

The Stefan Meyer Institute built a position sensitive Cherenkov light detector, based on SiPMs. The medium in which the Cherenkov photons are generated is not part of the device. This prototype consists of an array of 64 SiPMs and a light concentrator on top. The purpose of the light concentrator is to increase the sensitive area of the detector. In previous work, the light collection efficiency and uniformity has been tested for a chromium coated light concentrator. The module was scanned with a laser beam with a wavelength of 407 nm, a beam spot size of about 1 mm and a step size of 500 μm [3].

The task of this thesis was to scan the detector prototype with an aluminium coated light concentrator. In addition, the resolution of the scans was improved in regards to stepping size and beam spot diameter.

In a completely new setup, the scan was also performed with a tilted beam for the first time. The scans serve to test the light collection efficiency of the SiPM array in combination with an aluminium coated light concentrator as a function of different beam angles. The main interest of the results and the motivation behind the scans is the question, if such a light concentrator can really efficiently increase the sensitive area of a sensor and in what way that collection efficiency depends on the angle of the incident light.

This diploma thesis gives a detailed description of the tasks and research performed in order to measure the collection efficiency and uniformity of the SiPM array in combination with the aluminium coated light concentrator. The work is presented in the following chapters:

- Chapter two gives a short overview about the working principle of SiPMs and introduces the position sensitive SiPM Cherenkov detector.

- In chapter three, the experimental setup is described. This includes the light source, the way the optical setup was built to guarantee a small beam spot size on the detector, the setup of the motors and the settings of the detector itself.

- An important task for the scan was to write an automation routine, so that the position change of the beam spot on the detector and the data acquisition could be done automatically. The automation program is explained in chapter four.

- Chapter five presents the results for the performed measurements and gives detailed information about the data acquired during the scans.

- The sixth chapter gives a discussion about the uniformity of the scanned light concentrator funnels and compares the measured light collection efficiency to simulations

- Finally, a short summary and conclusion of the work is presented in chapter seven.

2. SiPMs and the position sensitive Cherenkov detector

2.1. Silicon Photomultipliers

Silicon photomultipliers (SiPMs) are solid state photon detectors, based on the principle of single photon avalanche diodes (SPADs). An avalanche photodiode (APD), as well as a single photon avalanche diode, uses the p-n junction of a semiconductor as a diode, operated in reverse bias. Increasing the reverse voltage causes the depletion region of the p-n junction to increase (thus the semiconductor becomes an insulator). In addition, the electric field of the p-n junction increases and causes the charge carriers (electrons and holes), that get produced due to the photoelectric effect, to accelerate and create an avalanche of secondary electrons (and holes) by impact ionization. At a certain applied reverse voltage, the p-n junction breaks down and a large current is created. This voltage is called breakdown voltage [4]. A more detailed description of the theory and illustrations of semiconductors and diodes can be found for instance in [5], [6] or [7].

Unlike APDs, SPADs work at a constant current and at a reverse bias which is larger than the breakdown voltage, this operating mode is called Geiger mode [8]. In SPADs, the bias voltage and the high doping produce a very large electric field (of about 10^5 V/cm [9]), so that any produced electron-hole pair leads to an avalanche of electrone-hole pairs and a discharge within the diode. In the event of an avalanche discharge, the quenching circuit (which consists of a quench resistor in the order of 100 kΩ [10]) causes the voltage of the diode to decrease below breakdown voltage thus stopping the avalanche. The SPAD can begin to detect photons again only after quenching the avalanche so that the bias voltage can rise again above the breakdown voltage. The time it takes for the bias voltage to rise above the breakdown voltage is called the "recovery time" and depends on the size of the SPADs and the circuit in terms of quenching resistor and SiPM capacitance. The larger the SPAD area, the longer is the "recovery time" [11].
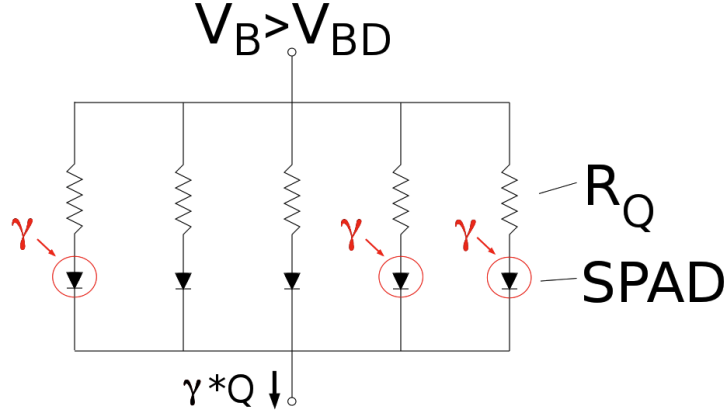
Figure 2.1.: Equivalent circuit of a Geiger mode APD (SPAD) in series with a quenching resistor (R_Q), connected in parallel. The output charge equals the number of fired SPADs ($\gamma*Q$). Compare to [12] and [13].

To achieve a recovery time in the order of $10 - 100$ ns and a large active area, several SPADs are connected in parallel (see figure 2.1) on a common substrate. The matrix of SPADs is called silicon photomultiplier (SiPM) and each SPAD is referred to as a pixel (as will be done in this document). In principle, a SiPM works like a SPAD, so each pixel/SPAD operates above the breakdown voltage. The output signal of the SiPM is the sum of the signals of each pixel. One pixel can only detect one photon at a time, however it is possible to detect several photons with the SiPM, because it consists of several pixels (SPADS). Single photons can also be detected. Figure 2.2 illustrates the pulse height spectrum of a SiPM. The spectrum consists of well distinguishable peaks, where each photoelectron (p.e.) peak corresponds to the number of pixels that discharged and thus sent a signal that is measured in mV. The pedestal corresponds to the noise of the electronics.

The efficiency of a SiPM is given by two factors: The fill factor is defined by the ratio of the active (actual detection) area of the SiPM over the total area of the SiPM. The photon detection efficiency (PDE), is the product of quantum efficiency (Q_E), triggering probability (P_T) and geometric efficiency (G_E):

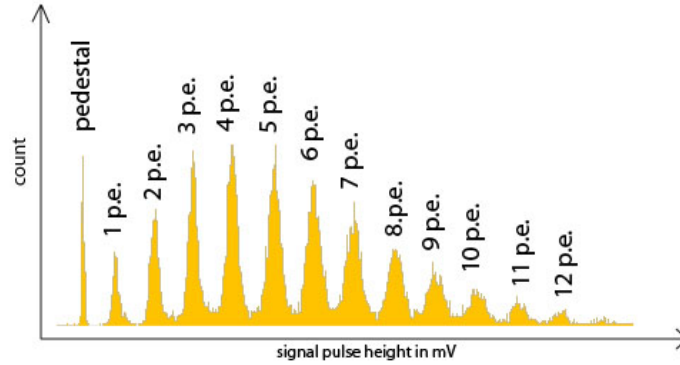$$PDE = Q_E * P_T * G_E \tag{2.1}$$

Figure 2.2.: Pulse height diagram of a SiPM. The photoelectron (p.e.) peaks correspond to the number of pixels that triggered a signal. The pedestal corresponds to the electronics noise.

The quantum efficiency (Q_E in equation 2.1) is defined as the probability for a photon to generate an electron/hole-pair in the p/n-junction and the triggering probability (P_T) is the probability for a charge carrier to initiate an avalanche during its passage through the electrical field while the geometric efficiency (G_E) (also known as *"fill factor"*) is the ratio of active over the inactive area of a pixel and thus is only dependent on the SiPM design.

Features of the SiPM technology are the single photon detection, a large gain in the order of $10^5 - 10^6$, a good pixel-to-pixel uniformity and an insensitivity to magnetic fields. In addition, SiPMs can operate at lower bias voltages (between 20 V and 70 V) compared to $100 - 200$ V for APDs (or kV for PMTs). These properties make SiPMs suitable for many research fields where photo detection is of great importance, such as particle and nuclear physics, astrophysics or medical imaging.

One disadvantage of SiPMs that originates from the high reverse bias voltage and poses a challenge for detector construction is the dark count rate. This noise appears due to thermal excitation and cannot be distinguished from a real photon detection signal. Dark count rates are of the order of $100 - 1000$ kHz and depend on the temperature of the SiPM and the applied voltage. Further information about the principle of SiPMs and their possible applications is given for example in [14], [15], [16], [17] and [18].
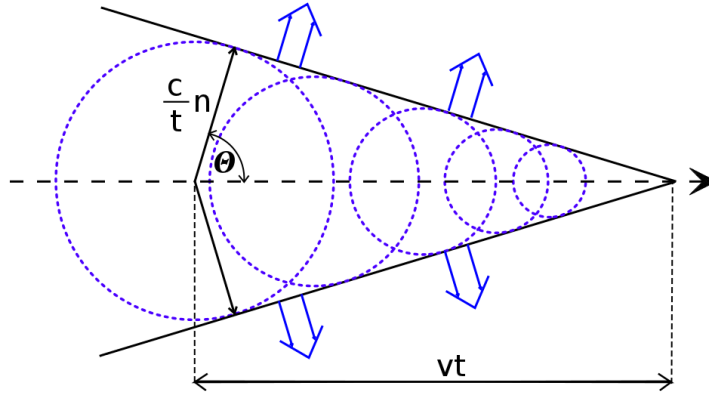
Figure 2.3.: Electromagnetic shockwave produced by a charged particle that travels through a medium faster than light in that medium [19].

2.2. Position Sensitive SiPM Cherenkov Detector

The photon detection system that was used in this experiment is based on the SiPMs described in section 2.1. This detector is a prototype that was developed and built at the Stefan Meyer Institute in Vienna. The detector is designed for position sensitive measurements by detecting Cherenkov light. The Cherenkov effect arises when a charged particle passes through a medium with a velocity faster than the velocity of light in that medium. The particle then emits photons on a cone, comparable to the faster-than-sound shock-wave. The conical shape of electromagnetic shock-wave, that is emitted by the charged particle, has a well defined half opening angle Θ. The emitted photons are called Cherenkov light or Cherenkov radiation [19]. Figure 2.3 illustrates the shock wave and the angle Θ, at which the shock wave is emitted. The angle Θ is given by

$$cos\Theta = \frac{1}{\beta n(\omega)} \tag{2.2}$$

where β equals $\frac{v}{c}$ (the particle velocity divided by the velocity of light) and n(ω) is the refractive index of the medium for the emitted radiation frequency. The angle is dependent of the velocity of the particle (and the frequency of the emitted radiation). This dependence is used in particle physics, where position sensitive photon detectors are used to detect the ring of the Cherenkov cones. With an exact timing information it is possible to extract the angle of the Cherenkov cone and thus calculate the velocity of the particle. To calculate
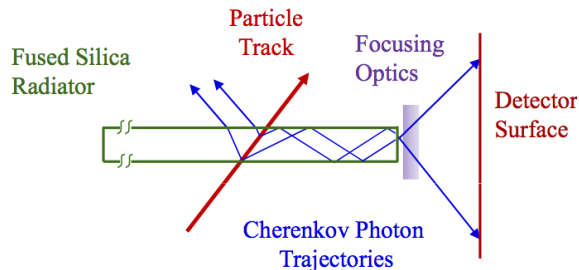
Figure 2.4.: Working principle of a DIRC detector [21].

the mass and to identify the particle it is also necessary to measure the momentum of the particle, which can be done with tracking detectors. A more thorough description of Cherenkov light detectors, including graphics is given in [1].

The prototype position sensitive Cherenkov detector is intended to be used for the barrel DIRC (Detection of Internally Reflected Cherenkov light) detector at the PANDA experiment at the FAIR facility in Darmstadt, Germany [20]. A DIRC detector uses the Cherenkov photons emitted by a charged particle that traverses a radiator. Some of the photons (those reaching the radiator surface with an angle larger than the critical angle $\Theta_c = arcsin(n_2/n_1)$ with $n_{1,2}$ being the refractive indices for the respective medium) get totally internally reflected, as can be seen in figure 2.4. The photons that finally exit the radiator then pass focusing optics like lenses or mirrors. After passing an expansion region, they finally get detected by a photon detector array, like the array presented in this work. The magnitude of the half-opening angle Θ is conserved, so accurate information about the particle velocity can be retrieved.

Further information about the PANDA experiment and the principles of the barrel DIRC detector at PANDA can be found for instance in [21], [22] or [23].

For the position sensitive Cherenkov detector, the SiPMs were arranged in an array of 8×8 chips, each chip having a separate output, giving a total of 64 signal channels for the detector. It must be emphazised that although a SiPM sensor can detect single photons, the precise point of impact on the sensor is not known. This means that with SiPMs, position information can only be acquired by arranging several sensors into an array and reading out which SiPM sent the signal.

A thorough analysis of different kinds of SiPMs was performed to find the best suitable

SiPM for the detector prototype. The results of this analysis are presented in [13].

The sensors finally used for the detector prototype are 64 SiPMs from Hamamatsu (S10931-100P). Each sensor contains 900 pixels with each pixel having a surface area of 100×100 μm^2 resulting in a total active area of 3×3 mm^2. These sensors were chosen because they have a high fill factor (which is the ratio of the active area of a pixel compared to the total pixel area) of $\sim 78.5\%$ and because they can be arranged in a compact manner due to their small housing. Table 2.1 shows the main characteristics of the used SiPM sensors.

Table 2.1.: Characteristics of the Hamamatsu 10931 SiPM [24]:

	Value	**Unit**
Pixel Size	100×100	μm^2
Pixel Number	900	
Active Area	3×3	mm^2
Fill factor	78.5	%
Peak sensitivity wavelength	440	nm
Operating voltage range	70 ± 10	V

The SiPMs are connected to 4 preamplifier modules, that were also developed in house. These preamplifier modules are based on the Photonique AMP-0611, however the in-house developed boards have 16 output channels each instead of one. Additionally, the input transistors were modified to achieve a better amplification gain. Using 4 modules with 16 channels each has the advantage, that they could be produced compactly with an area of 69.9 ± 0.01 $mm \times 43.6 \pm 0.01$ mm each and thus wouldn't take much space in the detector housing.

To reduce the cost of the detector while providing sufficient position resolution, the sensors were arranged with a certain space between them (see figure 2.5) and a light concentrator was developed to be put on top of that array. Using such a light concentrator has several advantages: First, the active area of the sensors is increased; thus a certain detection area is achieved with a smaller number of sensors, which reduces the total costs for the SiPMs. Second, increasing the active area without actually increasing the area of the SiPM improves the signal-to-noise ratio [25], because noise can only occur from within the SiPM itself, not from the additional active area. Third, with using fewer SiPMs, less read-out electronics is needed, thus allowing the detector to be built more compactly.
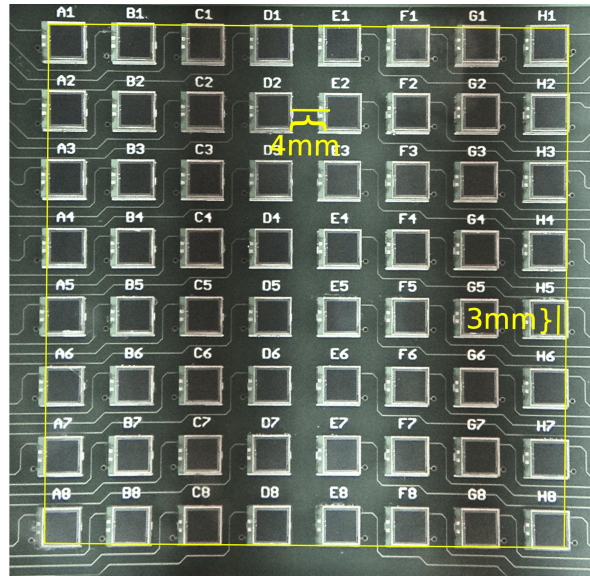
Figure 2.5.: SiPM board with visible active area (SiPM sensors) and inactive area. The array has s spacing compatible with the exit holes of the light concentrator, which is put on top of the array and guides the light to the SiPMs.

The light concentrator consists of 64 pyramid-like funnels with an area of $7 \times 7 \; mm^2$ on the entrance side and an area of $3 \times 3 \; mm^2$ on the exit side which is adjacent to the SiPM sensors. The light concentrator used in this setup is made out of brass and was coated with a chrome layer and an aluminium layer on top. Figure 2.6 illustrates an engineering drawing of the light concentrator with exact measurements as well as a photograph of the light concentrator.
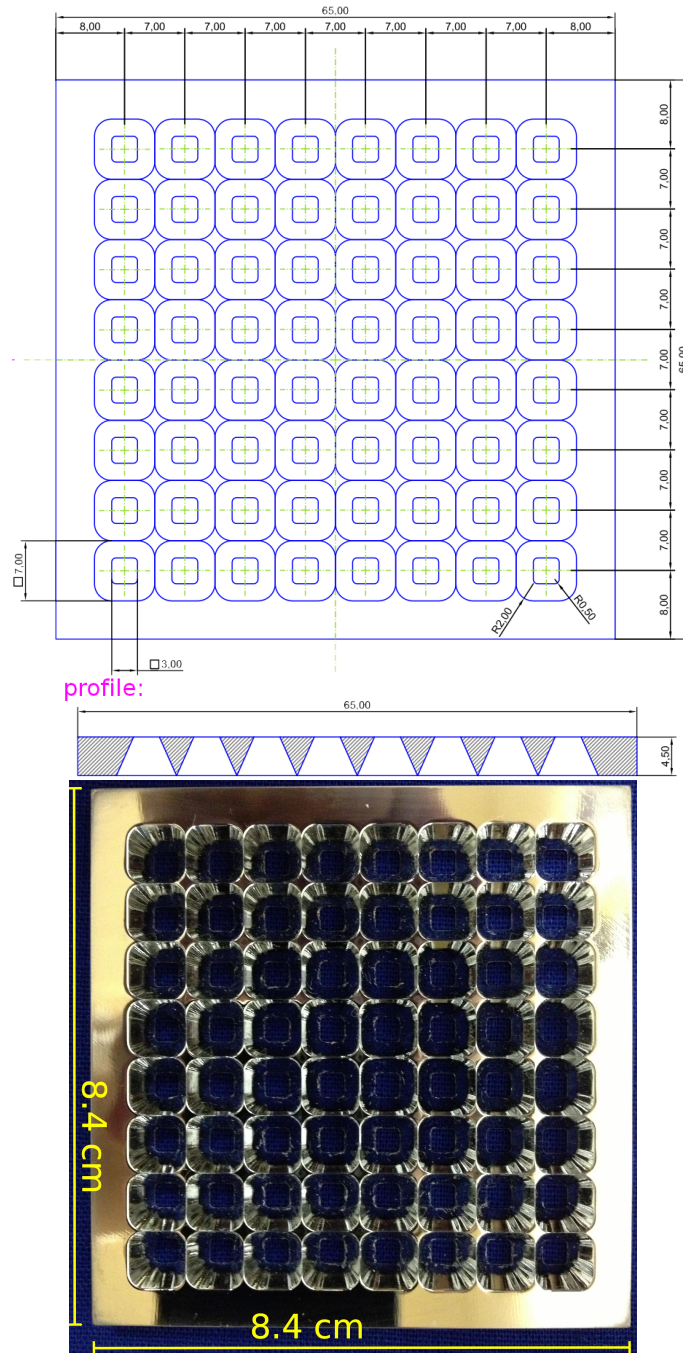
Figure 2.6.: Engineering drawing of light concentrator, curtesy of Doris Stückler, SMI (top) and photograph of light concentrator (bottom).

3. Experimental Setup

3.1. Laser Diode

As mentioned in chapter 2.2, the detector's purpose is to detect Cherenkov light. Since the number of photons emitted per unit wavelength per unit length of the medium through which the charged particle passes is inverse proportional to the square of the wavelength (see equation 3.1), more photons with shorter wavelengths get emitted [19]. This is why Cherenkov radiation is observed as bright blue light and since the Hamamatsu 10931 SiPM has the highest detection efficiency at a wavelength of $\lambda = 440$ nm (blue light), these sensors are (reasons provided in chapter 2.2) ideal for this type of measurements.

$$\frac{d^2N}{d\lambda dx} \propto \frac{\eta}{\lambda^2} \tag{3.1}$$

The initial idea was to use an existing laser with a wavelength of 404 nm, which is around the maximum of the photon detection efficiency. However, using an LED as photon source was easier to implement and also sufficient for these measurements since determining the timing of the photon signal was outside the scope of this project. This LED (`Toyota Gosei E1L31 - 3BOA2 - 02`) has a wavelength range of $465\,nm < \lambda < 475\,nm$.
The LED doesn't emit a continuous wave but pulsed light instead. This setup is chosen, because the SiPMs have got a certain recovery time ($100 - 200ns$ for an SiPM with an active area of $1\ mm^2$ and a pixel size of $100 \times 100\ \mu m^2$ [12]). During that time, the SiPMs are "blind" and thus can't detect any additional photon.
The pulse settings are the following:

- pulse rate: ~ 900 kHz

- pulse width: ~ 6.47 ns

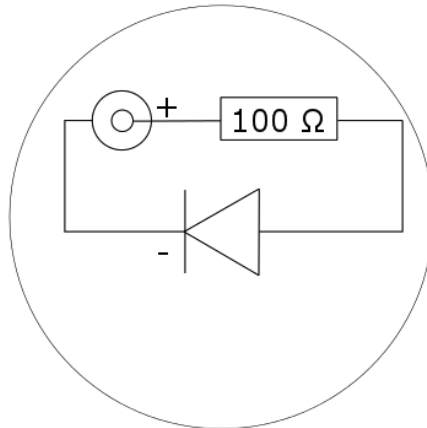- diode voltage: ~ 4.9 V

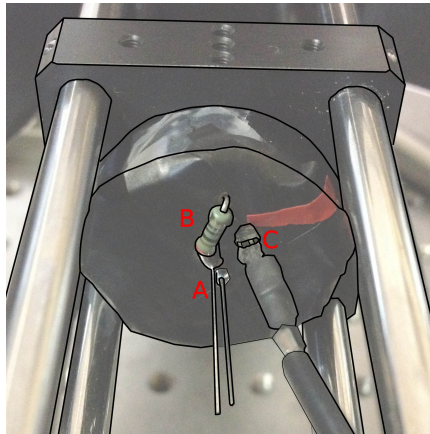Figure 3.1.: Circuit diagram of LED, resistor and connector.

Figure 3.2.: In this picture one can see the backplane of the working LED-circuit with (A) the connection wire of the LED, (B) the 100 Ω resistor and (C) a connector.

The diode was soldered onto a grid, together with a 100 Ω resistor and a connector. For an illustration of the circuit diagram see figure 3.1.

The grid has a circle-like shape so it could be fixed into one of the mounting plates, as can be seen in figure 3.2. Additionally, the diode bulb was fixed into a fiber adapter, cutting off most of the light that wasn't emitted into a forward direction.

3.2. Optical Setup

The beam emitted from the LED is $1.3 \pm 0.1\,mm$ wide, this diameter depends on the fiber adapter hole, in the experiment's case it's a `ThorLabs SM1FC` threaded fiber adapter. Taking the beam divergence into account, the beam area would probably be larger than the 3×3 mm² surface of the pixel photomultiplier, even when placed at a small distance from the SiPM.

As mentioned in chapter 2.2, one SiPM chip has a surface of 9 mm² and a pixel size of 100 μm times 100 μm. These dimensions imply that a laser beam with a very small beam diameter is beneficial for the goal of the experiments. This paragraph describes the setup that was chosen to reduce the beam diameter to the order of 100 μm.

As one can see in figure 3.3, the light is first emitted by the LED itself, the beam is already limited to a certain divergence angle by the fiber adapter (A). This fiber adapter also helps keeping the optical axis at the same position as the lenses and the pinhole. The beam is then sent through the first biconvex lens, with a focal length of 30 mm (B). The next optomechanical item, the pinhole (C), was put into the focal point of the precedent lens. The pinhole has a diameter of 10 μm and serves as a point-like light source. The beam then passes through two lenses (D, E). The first one is a biconvex lens with a focal length of 100 mm that collimates the beam. The second biconvex lens has a focal length of 200 mm. This lens is used to focus the collimated beam onto the silicon photomultipliers at a distance of 20 cm. All optical items (lenses, pinholes) were fixed in mounting plates by `Spindler & Hoyer (Linos)`.
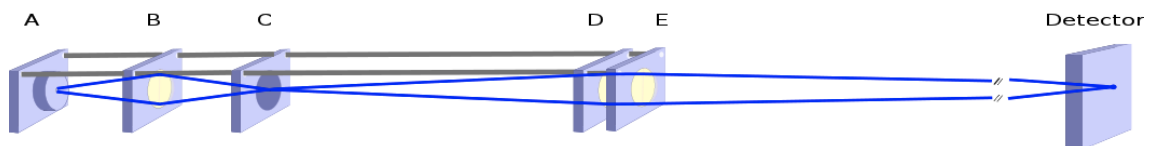

Figure 3.3.: Schematic of optomecanical items and laser beam.

ad fig. 3.3.: A: fiber adapter which limits the divergence of the LED beam
               B: biconvex lens with focal length 30 mm
               C: 10 μm pinhole which serves as point-like light source
               D: biconvex lens with focal length 100 mm, serves as collimating lens
               E: biconvex lens with focal length 200 mm, focuses the beam onto detector

After the scans had been finished, the beam diameter at the focal point was measured with a `ThorLabs PM100, S120A Silicon Sensor` power meter, a razor blade and a micrometer translation stage. Drawing 3.4 shows how the measurement works. For the measurement, a razor blade is fixed onto a translation stage (a razor blade was used because it has a very sharp edge without dents). The razor blade sits parallel to the focal point of the photon beam while the power meter is found about 3 cm further downstream from the razor blade mounted on the optical table. The beam's power is measured with the power meter in nano Watts. For these measurements, the razor blade is moved into the beam with a step size of $10 \ \mu$m. The laser power as a function of position is plotted and analysed using `QTIPlot 0.9.7.3` so that the beam spot size can be determined. See chapter 5.1 for results.
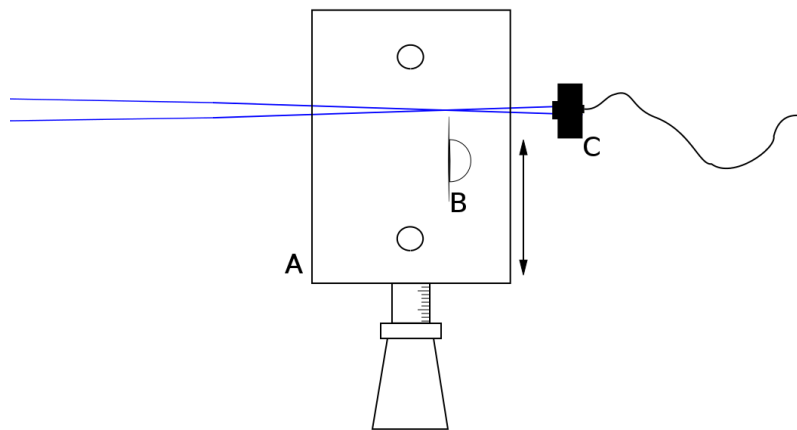
Figure 3.4.: Schematic of beam diameter measurement with a razor blade. A) is the micrometer translation stage, B) is the razor blade and C) the power meter.

3.3. Motor Setup

As will be explained in chapter 4.2, it is possible to take data of three SiPMs in one experimental run. These three chips together with the light concentrator have a total width of 21 mm and a height of 7 mm so a movement range of more than 21 mm is necessary. Also, one has to consider that in order to perform a scan of a SiPM sensor, it is necessary to move the laser beam by steps as small as $100\,\mu$m. The small stepping size of $100\,\mu$m is due to the pixel size ($100 \times 100\,\mu$m^2) of the SiPMs.

The stepping motors used were produced by `Physikinstrumente (PI)`, models `M-229.25S`. Both stepping motors are controlled via `C-663 Mercury Step Controllers`. Communication between the controllers and the computer works via USB (PC to controller) and daisy chain (controller to controller). `LabView` VIs were provided by the manufacturer to control the motors. In addition PI provided a program that allowed direct and simple communication to the actuators. For the experimental runs only LabView VIs were used. The main VI will be described in the section 4.1. In addition, the PI's program `PIMikroMove 2.8.0.3` was used to move the actuators to the starting or end position when manually adjusting the position of the detector.

The motors have a displacement range of 25 mm and a minimal step size of $1\,\mu$m; their maximal push/pull force is 50 N. This force is rather powerful for such an exact device, however it was necessary to make sure that no lateral forces affected the motor tip as those forces reduce the guiding accuracy and could damage the actuators [26]. That is why the weight of the combination of optical setup and motor setup has to be poised, minimising lateral forces on the motors' tips.

In this text, the coordinate convention is defined the following way: The x- and z-axis build a plane parallel to the detector surface plane, whereas the y-axis is parallel to the light beam. This means that the scan was performed in an x-z-plane, so one motor had to be mounted in a way that it could change the laser beam's position in z-direction (vertical), whereas the other was mounted in a way that it would change the beam's position in x-direction (horizontal). The motors and optical elements are fixed with stage posts onto an optical table. The drawing in figure 3.5 shows that the weight of the whole apparatus rests on the tip of the z-direction motor (yellow motor tip, (a)). This means that if the tip moves, the whole apparatus changes its position in z-direction. Additionally, one can see a post with cage plates at the cable-end of the x-direction motor (b). This setup serves as a stabiliser, reducing any wiggle (and thus change of the beam position on the detector),

caused by the upwards or downwards movement of the z-motor tip. These stabilisers also rest at the mounting-plate of the z-motor itself.
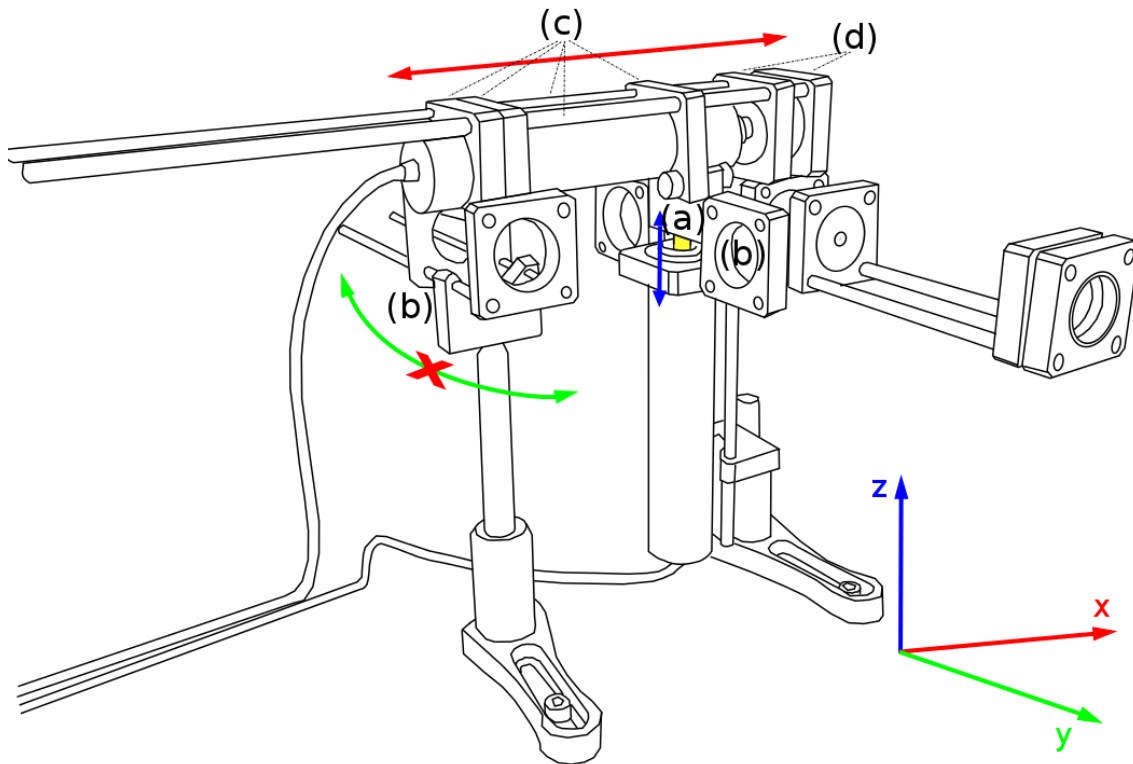

Figure 3.5.: Drawing of motor and optical setup. The tip on which all weight of the x-direction motor and the optical setup rests is marked in yellow.

ad fig. 3.5.: (a) z-axis motor tip on which the weight of the optical and x-axis motor rests
(b) cage plates that serve as stabilisers agains wiggling during z-axis move
(c) cage plates and connection rods that serve as weight and guidance
(d) fixation cage plates, fixed on optical apparatus and on x-axis motor tip

The x-direction motor is fixed via optical mounting plates onto the tip of the z-axis motor.

To balance the weight for both, the z-motor and the x-motor, the connection rods, together with cage plates fixed on the end of the x-axis motor serve as weight and guidance lines (c). The optical apparatus that was described in section 3.2 is mounted onto the x-direction motor, again with cage plates. The connection rods that connect the fixation cage plates (d) with the other three cage plates (c) are only fixed to the two front plates at the tip of the x-axis motor. This means that these rods have to be free to move through the other holes. To make sure that friction was reduced, the cage plates and rod were lubricated with a liquid called "WD-40".

3.4. Scanned sensors and detector settings

The collection efficiency of the light concentrator was determined by choosing at random, three adjacent SiPM sensors, labelled F2, F3 and F4. The position of these SiPMs is displayed in figure 3.6. It is important to understand that during the scans the module was rotated clockwise, so the alignment of the sensors was horizontal and not vertical as shown in the photo. Also, it is crucial for the measurements, that the complete experimental setup was mounted in a dark box, so only photons emitted from the diode could reach the SiPMs.
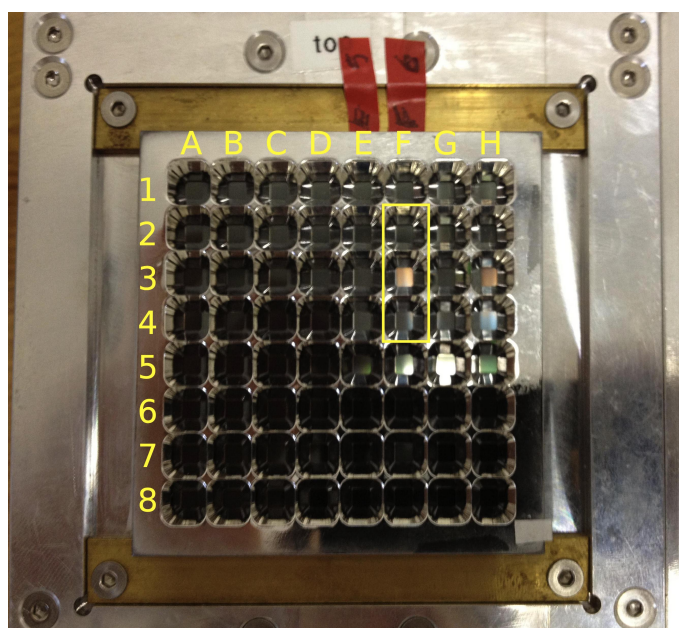
Figure 3.6.: Detector with light concentrator and highlighted SiPM sensors.

The detector works at a certain bias voltage that depends on the respective SiPM. For the development of the position sensitive detector, SiPMs by `Hamamatsu` were chosen. The `S10931-100` series sensors have the advantage that they have a rather high fill factor (78.5 %). Additionally, the 3×3 mm^2 sensor area in the very small housing allows for the compact arrangement, that was needed in order to align the SiPMs into a matrix of 8×8 sensors [13]. Hamamatsu offers these SiPMs with an operating voltage of 70 ± 10 V (see table 3.1 for more specifications). It is critically important to provide a constant current for all the sensors such that comparable results can be made between them. To set the operating voltage, the `ISEG EDS` module was used. This module is a voltage source which allows for variations in the current, which is not favourable for the operation of SiPMs as a constant current is needed. To achieve an operating voltage of ~ 70 V for each sensor while maintaining a constant current, the ISEG module was used and a current stabilizer (`Texas Instruments LM334Z`) was connected in series with each of the used ISEG channel to each of the three sensor channels. A circuit diagram of the current stabilizer is given in figure 3.7.

Table 3.1.: Characteristics of the Hamamatsu 10931 SiPM: [24]

	Value	Unit
Pixel Size	100×100	μm^2
Pixel Number	900	
Active Area	3×3	mm^2
Fill factor	78.5	%
Peak sensitivity wavelength	440	nm
Operating voltage range	70 ± 10	V

The current source devices were set at about $0.57\,\mu$A when measured with a multimeter, however the ISEG `CANHVControl` (voltage control program) measured lower currents of about $0.48\,\mu$A to $0.51\,\mu$A, depending on the respective channel and SiPM. Comparing the measured current from the beginning with the one from the end of each scan, one could see that the current only changed in the order of one nA (as compared to an order of 100 nA without the current source).

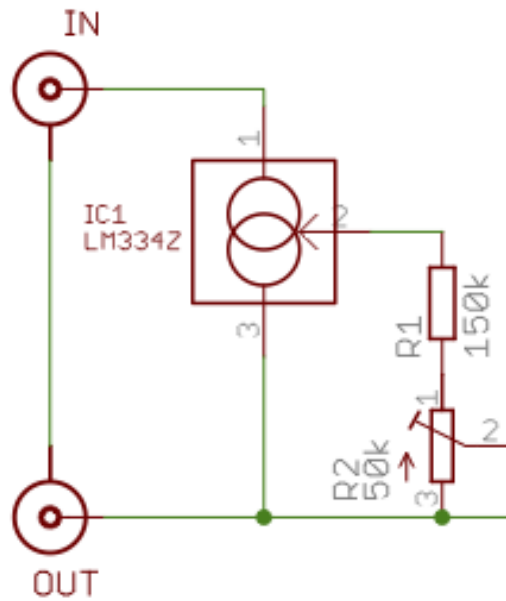The voltage for the MPPCs was set to 72 V for the three sensors respectively, but measuring

Figure 3.7.: Circuit diagram of the current source used, connectors and resistor, courtesy of Herbert Schneider, SMI.

the voltage with a multimeter after the current source showed that the voltage was of the order of 100 mV lower than that set voltage. The measured voltage values can be found in table 3.2.
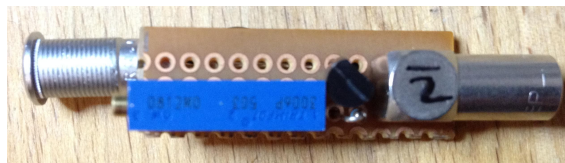

Figure 3.8.: Photo of one of the used current sources (blue), together with the LEMO connectors and resistor.

The in-house developed preamplifier modules were supplied with a voltage of 8 V and a current of about 220 mA per module. As huge noise was experienced when starting the first test scans, it had to be ensured that all LEMO-connectors (one for the preamplifier modules, one for the bias voltage and one for the signal for each channel respectively) were

Table 3.2.: Comparison of voltage set on the scanned sensors with ISEG module versus delivered bias voltage measured with a multimeter.

	F2 [V]	**F3 [V]**	**F4 [V]**
set	72.0	72.0	72.0
measured	71.85	71.53	71.92
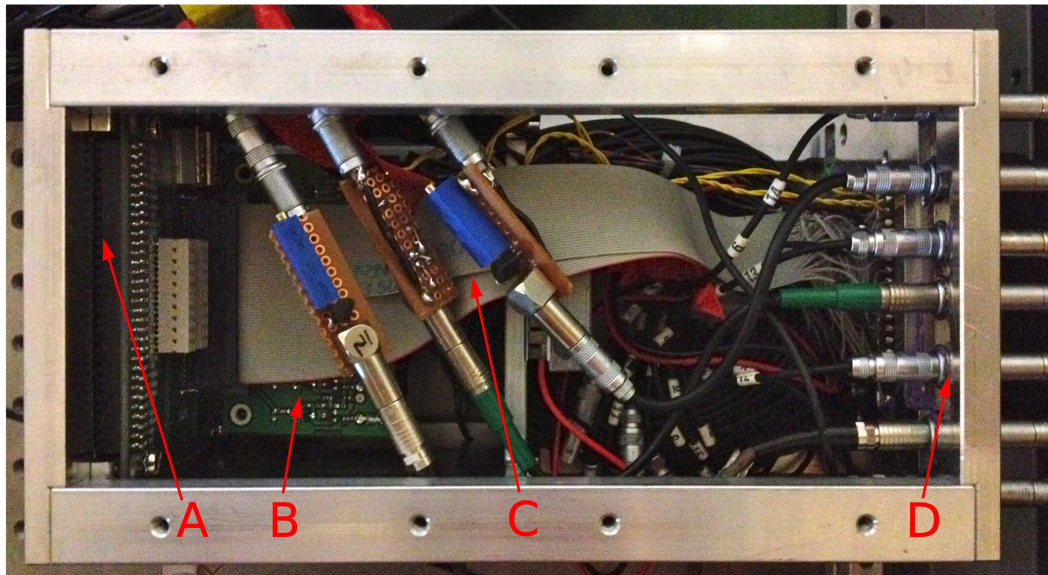
Figure 3.9.: Photo of the detector with open top. Attaching the LEMO connectors to the detector body (on right side of photo) reduced the noise that was caused by radio waves to an amplitude of 2 mV.

ad fig. 3.9.: A: backplane of SiPM matrix
B: backplane of the preamplifier module 2
C: 3 current sourcese
D: LEMO connectors attached to the detector body

set on the same ground. To achieve this, all but one preamplifier module (where one module has 16 signal channels) were removed, leaving enough empty space within the detector box to keep the complete length of all 16 signal cables inside that box.

The opening of all the 64 signal cables on the backplane of the detector was used to fix seven male-to-male adapters onto the detector, making sure that all connections were on the same ground. This resulted in a decrease in noise to an amplitude of about 2 mV instead of about 5 mV. Also, it has to be recognised that with this setup the detector only had two SiPM rows (E and F) being connected to a preamplifier module, sending measurable signals, instead of eight rows. For the application as position sensitive Cherenkov detector with all 64 SiPMs working, the cooling that was designed and implemented (Peltier cooling) should be used to reduce the thermal noise. This cooling wasn't used during the scans as the described approach gave sufficiently good results.

4. Automation and data acquisition

4.1. Automation

For this experimental setup, it is necessary to move the beam spot by a small step size
($100\,\mu$m) and repeat the measurement for each position for around 1000 times to obtain
good statistics. The light beam was scanned across the SiPM module using actuators while
data was acquired using an oscilloscope (`LeCroy WavePro 735Zi`). These experimental
requirements call for an automation program.

The most feasible way of writing such a program and combining hardware from different
manufacturers was to use `National Instruments' LabView` (version 8.6). The advantage
of LabView is that most manufacturers already provide the necessary drivers, thus reducing
the need of writing software by oneself. This "out of the box" solution was perceived to be
much faster than writing the communication protocols e.g. in a programming language like
C++.

The overall setup of the LabView VI (Virtual Interface), controlling the experiment is easily
explained:

Looking at the front panel (see figure 4.1), there are 3 masks controlling the actuators and
their settings. Looking from left to right the first mask, "Mercury Controller Setup", only
gives information about the communication between the actuators and the computer. As
will be explained in appendix A, this communication setup has to run each time the main
VI is started. In the mask "Mercury Movements" one can specify the origin for both axes,
so from which position the actuators start the movement. Additionally the step size gets
defined in this mask. The mask "Stopping Criteria" sets the end position for both axes and
reads the position of both controllers after each move. Note that the step size as well as
the start and end positions are given in mm.

The mask "Oscilloscope Settings" gives the possibility to select the correct parameters for
the data readout from the oscilloscope. The number of samples taken can also be set. For
more detailed information see section 4.2.

Furthermore one can find a "stop"-button on the front panel. This button can be used in case the program has to be stopped manually and guarantees that the connection to the actuators is closed properly.
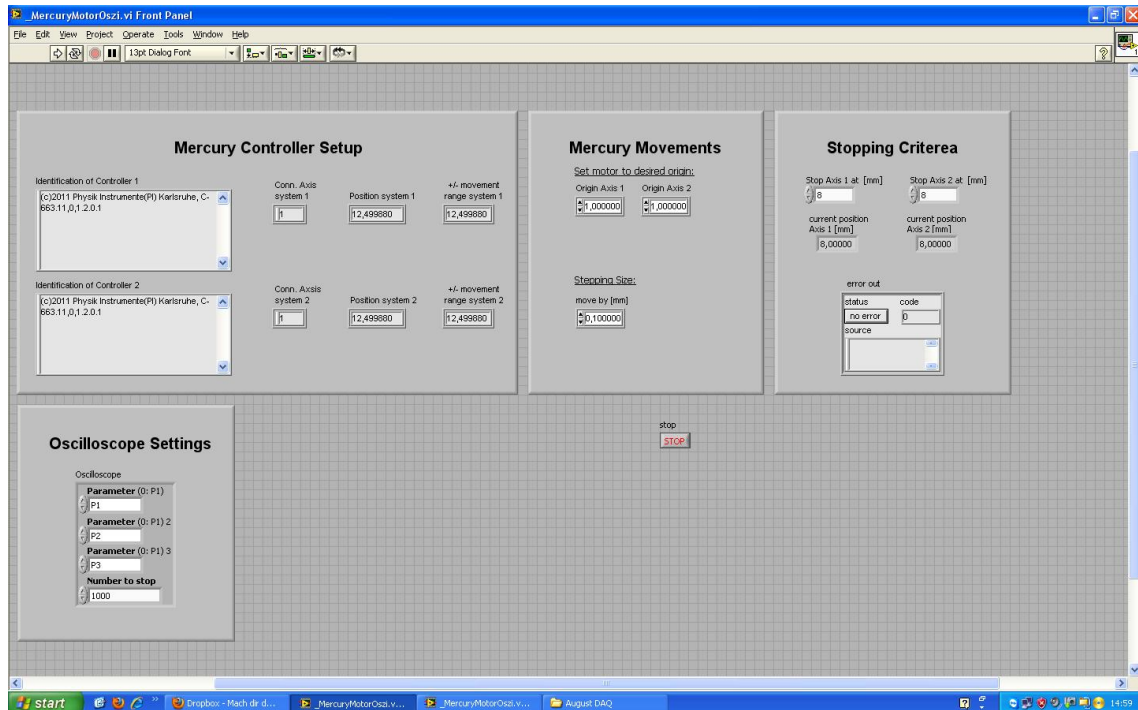
Figure 4.1.: Screenshot of the front panel of the main automation VI.

In this section, only an overview of the complete automation VI is given. For a more detailed description of the sub VIs and the illustration of the block panel, the reader is referred to appendix A of this text.

When starting the VI, the first command creates a simple text file. The user can specify the name and the location of the file. Then, the connection between PC, controllers and actuators gets established. This procedure has to be done every time the actuators are controlled with LabView and ensures proper communication between the devices and the computer. The sub VI for this setup is provided by the manufacturer and cannot be changed. After successful identification of the actuators the position of the LED beam is set to the origin. At the origin, the oscilloscope acquires the first data set. The specified oscilloscope data (see section 4.2) is written into the text file together with the coordinates

of the actuators (these coordinates reflect the position of the LED beam on detector).
The main routine of this VI consists of two nested while-loops, the inner one moving the
x-axis from the origin to the end position and the outer loop moving along the z-axis
from origin to the end position. The oscilloscope acquires data for each position and the
automation program writes it to a text file. The program ends as soon as both loops are
successfully completed or when the stop button is activated on the front panel.

4.2. Data acquisition

A four channel `LeCroy WavePro 735Zi` oscilloscope was used for data acquisition. Three of
the four channels were taken for data acquisition, while the fourth was used as trigger input
from the light source (see fig. 4.2). This means that only 3 SiPMs could be scanned in one
experimental run. The connection between the oscilloscope and computer was established
via a network connection.
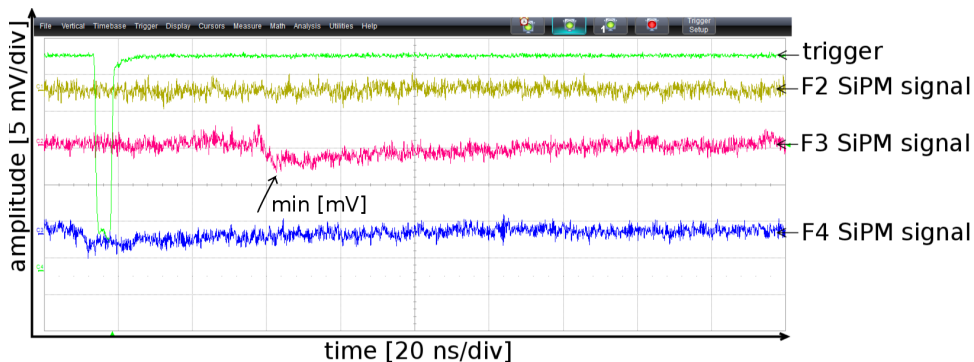
Figure 4.2.: Snapshot of data acquisition with the channels in yellow, pink and blue repre-
senting the respective signal from the three SiPMs and the channel in green
representing the trigger input. As the beam spot of the light source is very
small, only one SiPM sends a signal at a time, in this case the sensor F3.

The scope of the experiment was to extract the pulse height from the signal of the respective
SiPM. As the SiPM signal is a negative voltage (in the order of millivolts), the amplitude of
the signal was measured by acquiring the lowest point of each waveform with the oscilloscope
during the acquisition window of 200 ns. The parameter set on the oscilloscope is called
"Minimum (min)". To achieve good statistics, 1000 samples were taken per position of

the photon source for each of the three channels respectively. The oscilloscope was set to calculate the mean and standard deviation of the lowest value of the waveform for these 1000 waveforms (samples). The two values (mean and standard deviation) per channel were then sent to the computer and saved in the text file that was created at the beginning of each run. The VI that acquires the data from the oscilloscope and sends it to the computer is described in appendix A.2.1.

Figure 4.2 gives an example of the data acquisition with the oscilloscope. Channels 1 to 3 (depicted in yellow, pink and blue) are the measured signals for the three scanned SiPMs F2, F3 and F4. Channel 4 (depicted in green) is used as trigger input. The snapshot shows that the photons from the light source hit the F3 SiPM, resulting in a distinguishable signal (of the order of about -4 mV), while the other signals of the other two SiPMs only reflects noise.

5. Results

5.1. Beam Diameter Measurement

As described in section 3.2, the beam diameter was measured with a power meter and a razor blade. The position of the razor blade was changed with a micrometer translation stage by steps of 10 μm. Figure 5.1 shows the progression of LED power vs. position of the razor blade. Note that the absolute mm value of the position is arbitrary and based on the measurement setup. Only the relative μm position versus LED power is used for analysis.
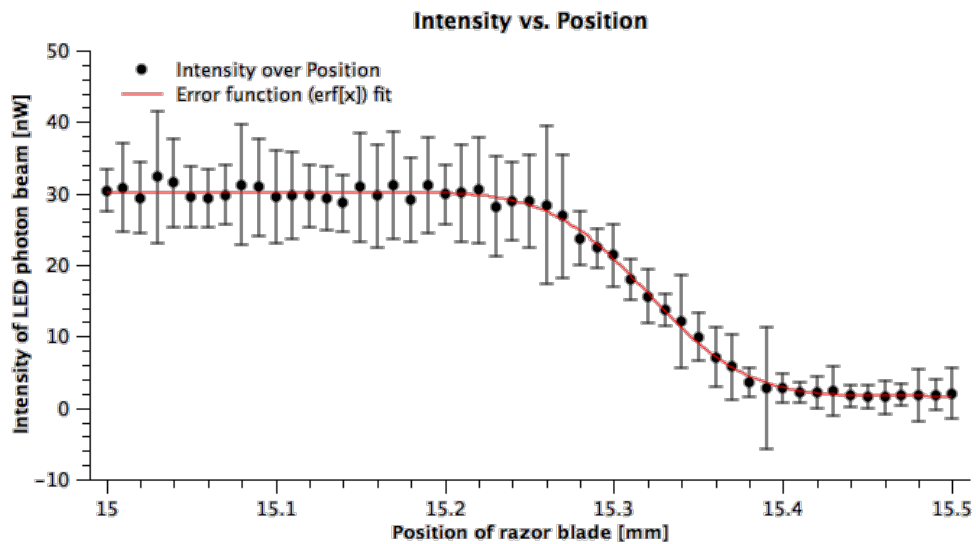
Figure 5.1.: Diagram of the position of the razor blade versus measured intensity of the LED beam. The complementary error function was fitted to the data.

Figure 5.1 illustrates the data from the power measurement. The profile resembles an integrated Gaussian profile, so the error function (actually the complementary error function (1-erf[x]), as this function is more accurate) was fitted to the data. The following fitting function, according to [27] was used to fit the data:

$$P_{measured} = P1 * \left(1 - erf \left(\frac{\sqrt{2}(x - P2)}{P3} \right) \right) - P4 \tag{5.1}$$

Here, P1 represents the maximum power measured and divided by 2, P2 represents the offset on the x-axis, P3 equals $w = 2\sigma$ and is used to calculate the full width half maximum (FWHM) of the beam spot diameter and P4 gives the offset on the y-axis.

Table 5.1.: Fit values of the error function of figure 5.1. $P1$ is the half the maximum power, measured, P2 is the x-axis offset, P3 is used to calculate the beam diameter, P4 is the offset on the y-axis.

	Value		Error
$P1$	14.27	$\pm$	0.153
$P2$	15.32	$\pm$	0.001
$P3$	0.092	$\pm$	0.004
$P4$	16.50	$\pm$	0.251

The data in figure 5.1 shows large error bars. The χ^2/doF of the fit is 0.58, indicating that the errors of the measurement are too large and cannot be only statistical errors. However, this measurement was performed to check if the beam spot diameter is of the order of a SiPM pixel (which is $100 \times 100~\mu m^2$), and the achieved degree of precision is sufficient for this purpose.

Figure 5.2 shows a plot of the error function and a Gaussian and how σ and w fit into those functions.

As mentioned above, the fitting parameter P3 $= w$ is used to calculate the beam spot diameter. The FWHM of the Gaussian distribution, on which the error function is based, is calculated with the equation 5.2:

$$FWHM = 2\sqrt{2ln2}\,\sigma \tag{5.2}$$
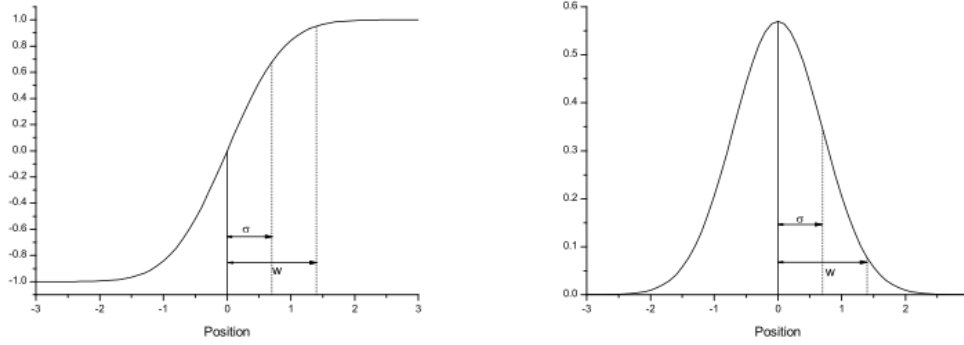
Figure 5.2.: Plot of the error function and the Gaussian distribution with σ and w, as presented in [27].

As $w = 2\sigma$, the equation transforms into $FWHM = \sqrt{2ln2}\ w$. Using the value and the error of parameter P3 from the fit (as shown in table 5.1), the beam diameter is measured to be $\mathbf{108 \pm 4\ \mu m}$. This is a good value for the experiment, as it implies that no more than four pixels of the SiPM were fired at a time.

5.2. Photon Number

The average photon number reaching the detector was estimated by using a laser with a wavelength of $\lambda = 404\ nm$, while directing the beam onto the three SiPMs that were used in the experiment. The oscilloscope is used to transform the sensor signal into a pulse height spectrum, as shown in figure 5.3. As this estimation only serves to cross-check the magnitude of the acquired signal during experiment, no offline analysis was performed. In an offline analysis the peaks of the pulse height spectrum would have been fitted with a Gaussian. The distance between two means of the fitted Gaussian then gives the single photon level. In this rough estimate, the respective mean of peaks of the spectrum was chosen manually, so no error can be provided. The histogram in figure 5.3 can identify the pedestal, which represents the noise (e.g. dark counts), the peak for single photon and for double photons. The tail of the histogram represents events when more than two SPADs fired. The single photon levels are given in table 5.2.

The values for the single photon level with the data from the experimental runs implies that on average, no more than two pixels were fired at any given time. Taking into account the LED beam diameter (108 μm) and the side length of a SiPM pixel (100 μm), it is very

Table 5.2.: Single photon level

	mean distance [mV]
F2	$\sim$ 2.40
F3	$\sim$ 2.25
F4	$\sim$ 2.45
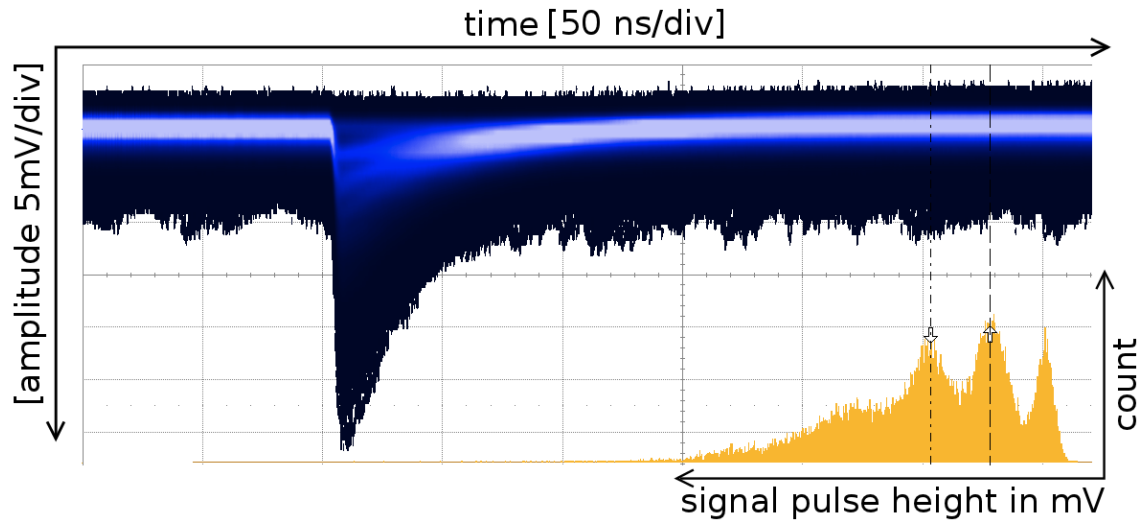
Figure 5.3.: Signal and pulse height diagram of F4 SiPM sensor.

likely that no more than one to four pixel triggered at a time as a response to the light beam.

5.3. Data Preparation

The scans were performed with three different settings:

- F2, F3, F4 were scanned separately with and without light concentrator

- F2, F3, F4 were scanned at once with and without light concentrator

- F2, F3, F4 were scanned separately with light concentrator and a changed beam angle of **14° 54′ ± 8′ 13″** in x direction

The data acquired during these scans was transformed into two-dimensional and one-dimensional histograms. The used routines are based on C and ROOT [28].

The $\sim 15°$ angle was used, because the opto-mechanical setup did not allow for any other angle in order to keep the focal point at the correct distance. The values that were taken during data acquisition are the minima of the waveforms for each channel. These values are negative millivolt values. The C routines, that were used to prepare and analyse the data, changed the sign of the mean values, so only positive values are presented although negative mean values were acquired.

In a first step to analyse the data, the noise levels for each channel was defined by calculating the mean of the last scanned row for each of the three photo sensors for the single scan and the first row for the triple-scan, as the light beam was positioned in a way that no light could have been detected by any of the three sensors. The noise per channel then was subtracted for each data point of the respective channel.

The noise-reduced data was used for each of the plots and for the calculation of the collection efficiency ϵ_{col} in chapter 5.4, unless it is stated otherwise. Figures 5.4a - 5.4c are the summation over all z. These projections show what the data would have been without noise correction. Sensors F2 and F3 have a significantly higher intrinsic noise than F4.

Figures 5.5a - 5.5f and 5.6a - 5.6c show the two-dimensional histograms of the data of the one and three sensor scans respectively. Each bin represents the mean of 1000 samples acquired at a certain position. Errors are not included.

The bird's-eye views of the histograms in figures 5.7a - 5.7c clearly show the structure of the SiPM sensors, of the light concentrator funnels and the impact on the light collection when the incident beam angle is changed. In addition, one can clearly distinguish between the areas where photons were detected and the areas where no photon detection took place.

In a next step the two-dimensional histograms of the three-sensors-scan were transformed into one-dimensional histograms. These projections were done in x-direction and in z-direction (see figures 5.8 and 5.9); error bars are included.

The projections show the signal height of the scans with light concentrator with and without incident beam angle (in red) compared to the signal height without light concentrator (in black). The projections shown in figures 5.8a - 5.8b give a good example of the homogeneity of the light concentrator.

An interpretation of the histograms will be presented in chapter 6, **Discussion**.
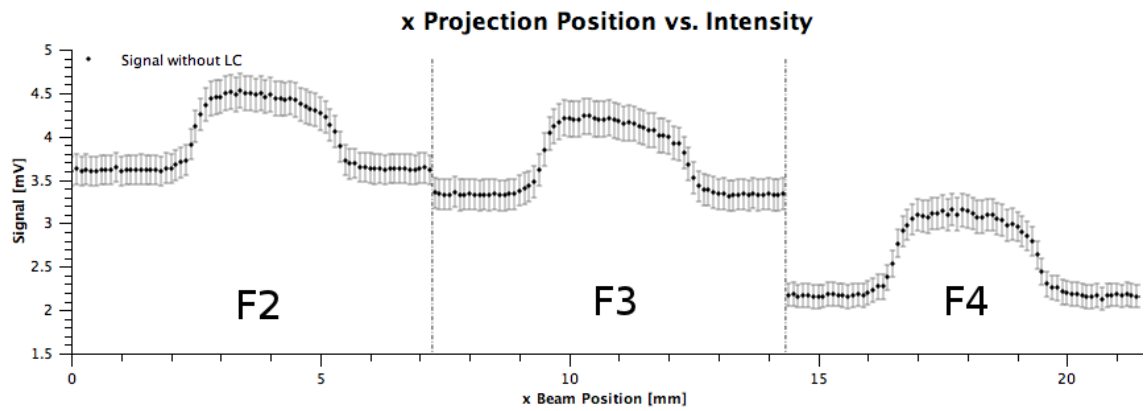
(a) Signal with noise, without light concentrator
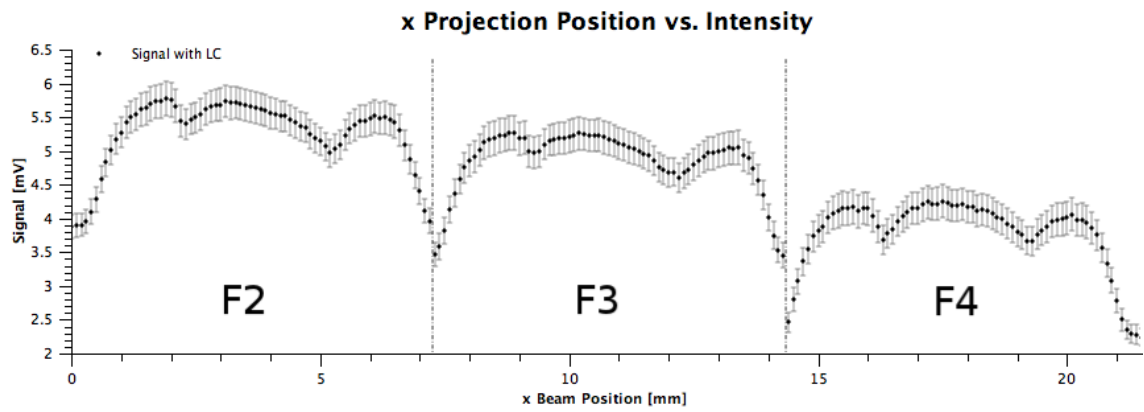
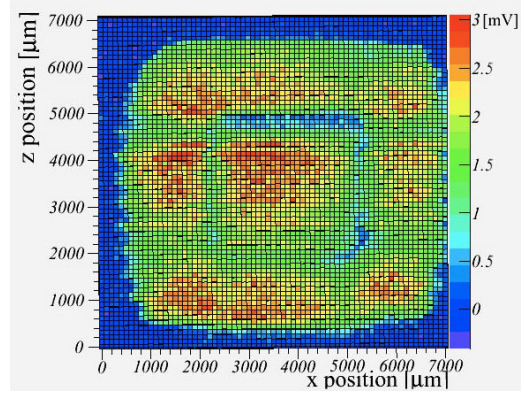(b) Signal with noise, with light concentrator
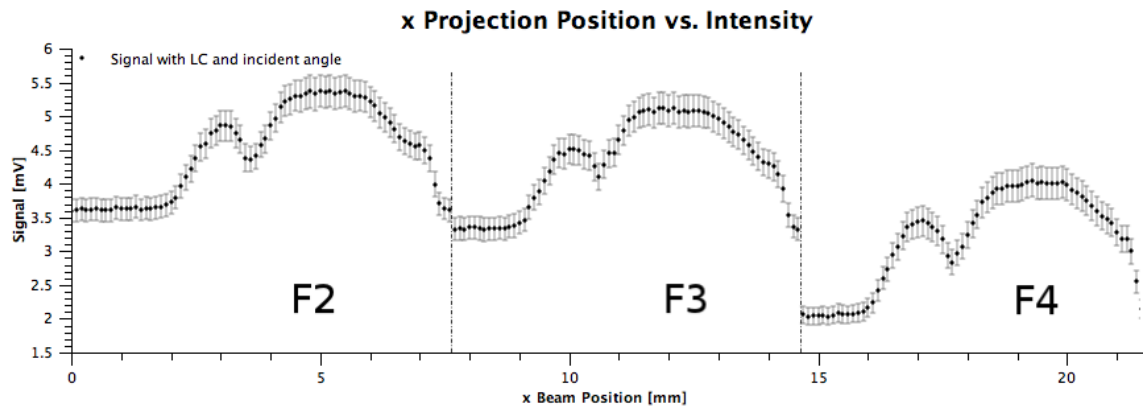
(c) Signal with noise, with light concentrator and beam angle of about 15°
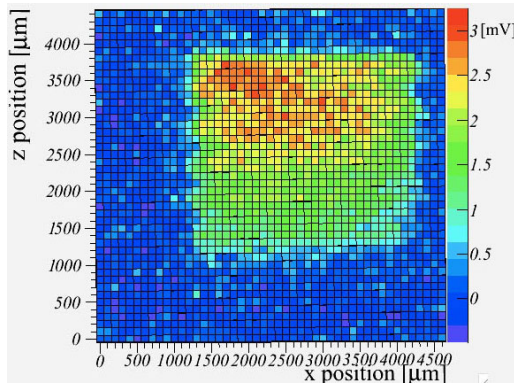
Figure 5.4.: X projection of the scan-data without noise correction for the 3 sensors F2, F3, F4 (a) without LC, (b) with LC and (c) with LC and an incident beam angle of about 15°.
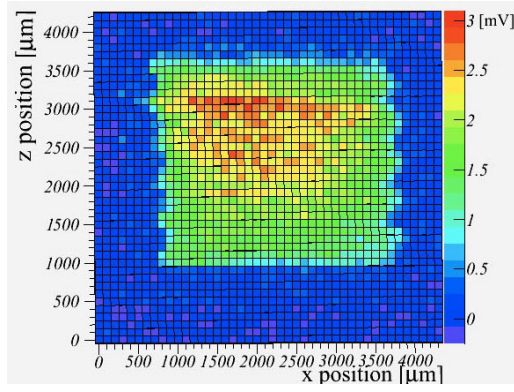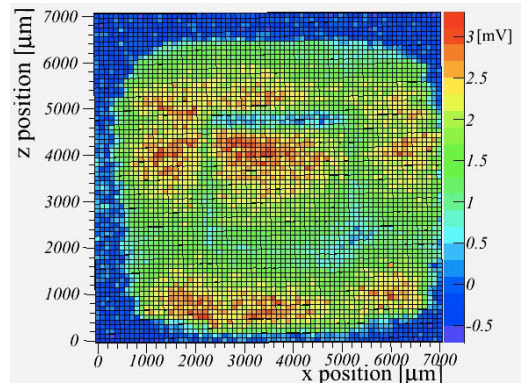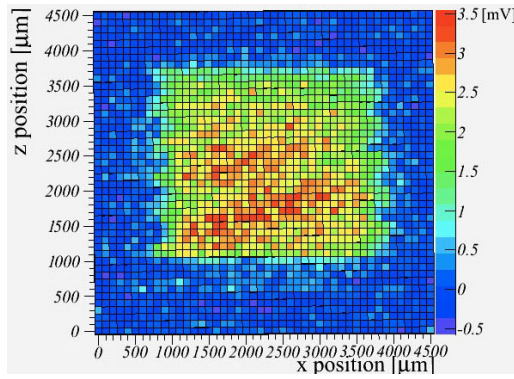
(a) F2 signal, without light concentrator
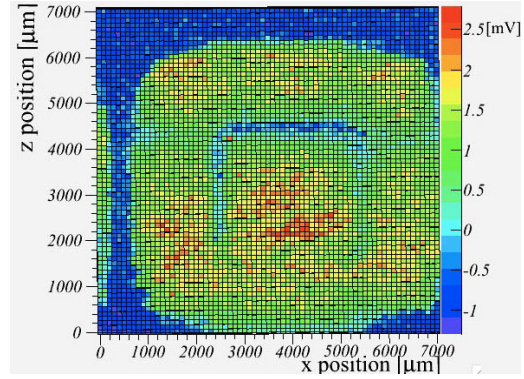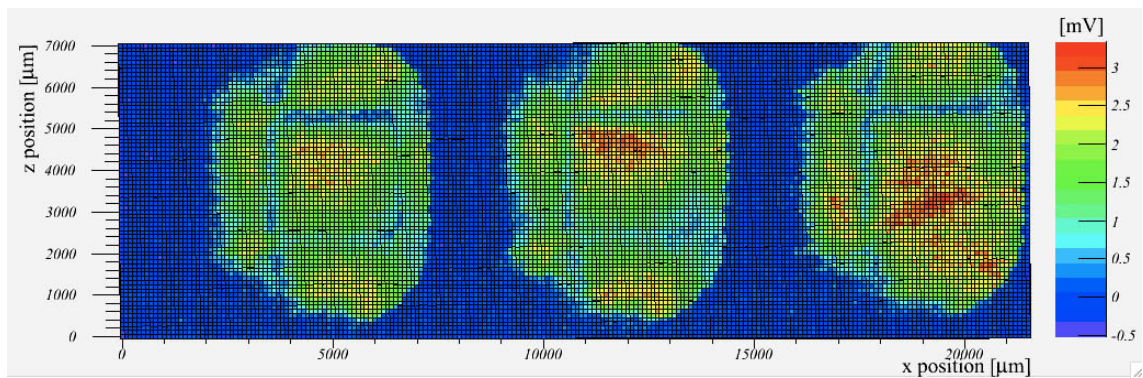
(b) F2 signal, with light concentrator

(c) F3 signal, without light concentrator

(d) F3 signal, with light concentrator

(e) F4 signal, without light concentrator

(f) F4 signal, with light concentrator

Figure 5.5.: Scans for the channels F2-F4 with (b, d, f) and without (a, c, e) light concentrator. The off-center position of the SiPMs in (a, c, e) has no influence on the calculation of the collection efficiency, as will be shown in chapter 5.4
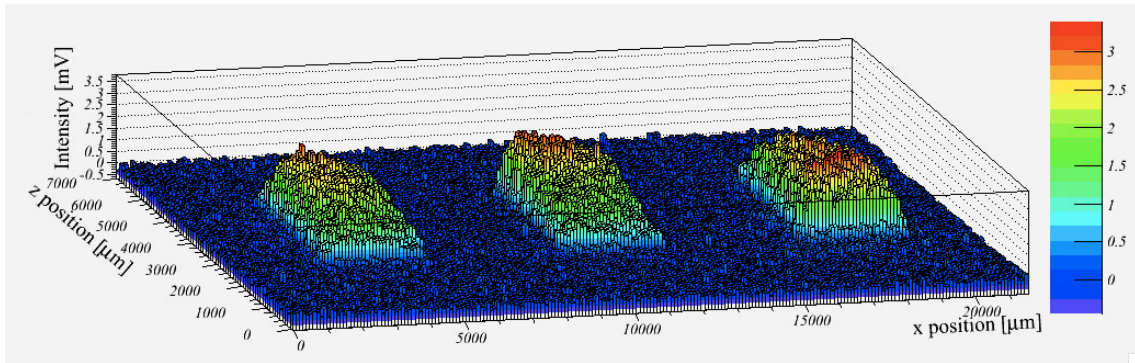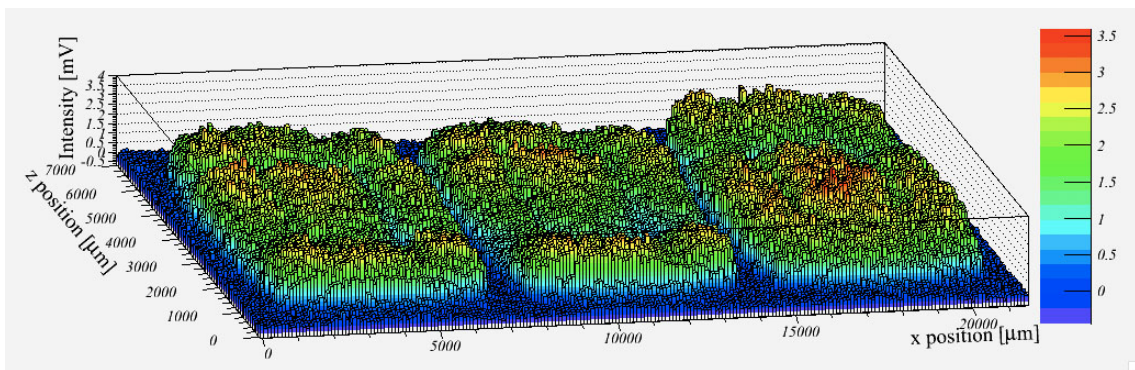
(a) Signal without light concentrator

(b) Signal with light concentrator
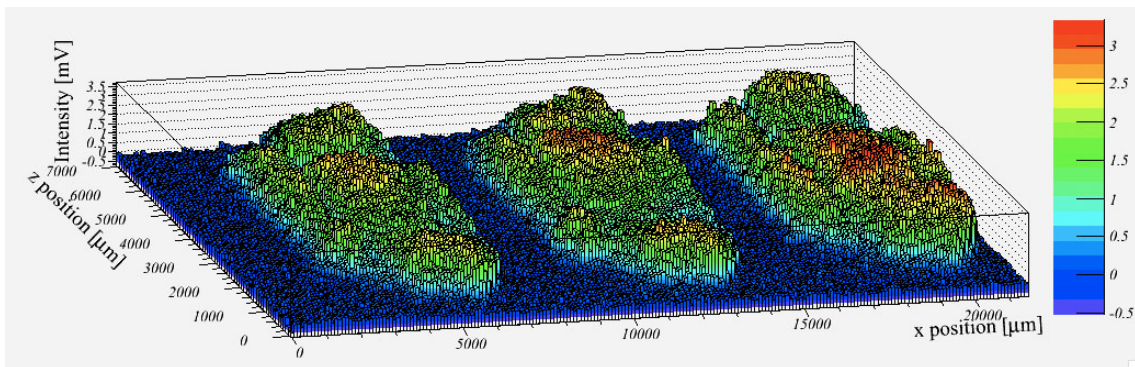
(c) Signal with light concentrator and beam angle of about 15°

Figure 5.6.: Two-dimensional histogram of the scan data for the 3 sensors (a) without LC, (b) with LC and (c) with LC and an incident beam angle of about 15°.
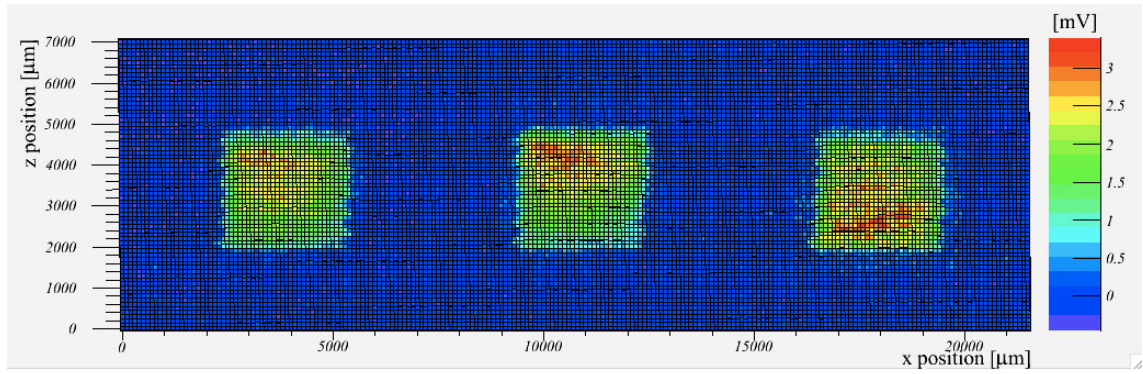
(a) Signal without light concentrator
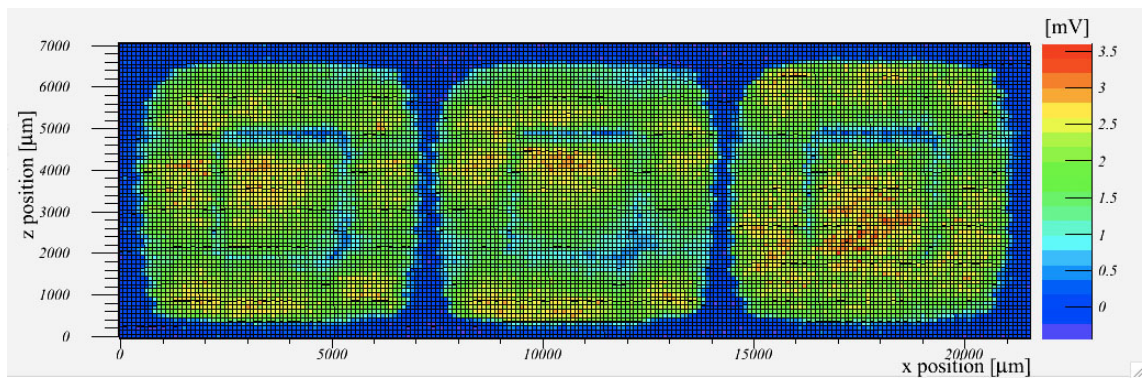
(b) Signal with light concentrator

(c) Signal with light concentrator and beam angle of about 15°

Figure 5.7.: Two-dimensional histogram of the scan data for the 3 sensors (a) without LC, (b) with LC and (c) with LC and an incident beam angle of about 15°.
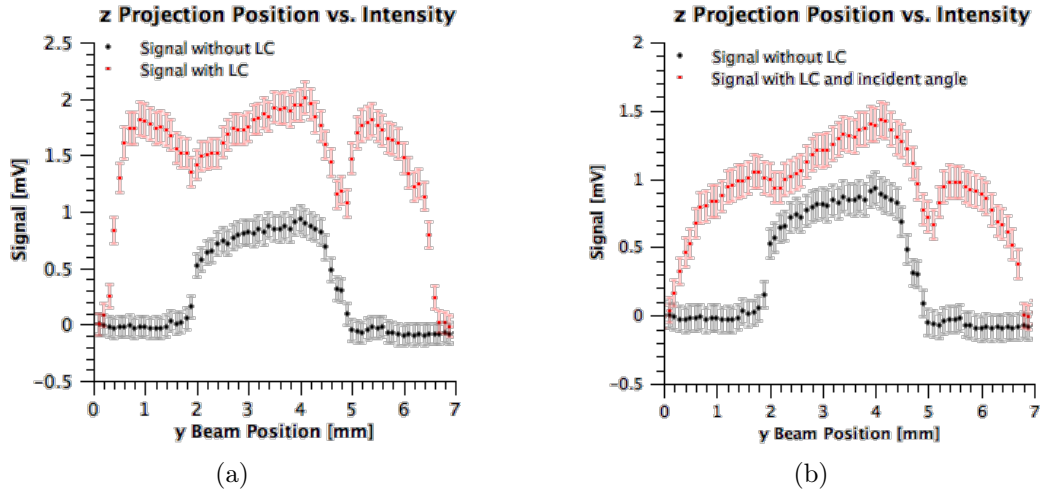
(a)

(b)
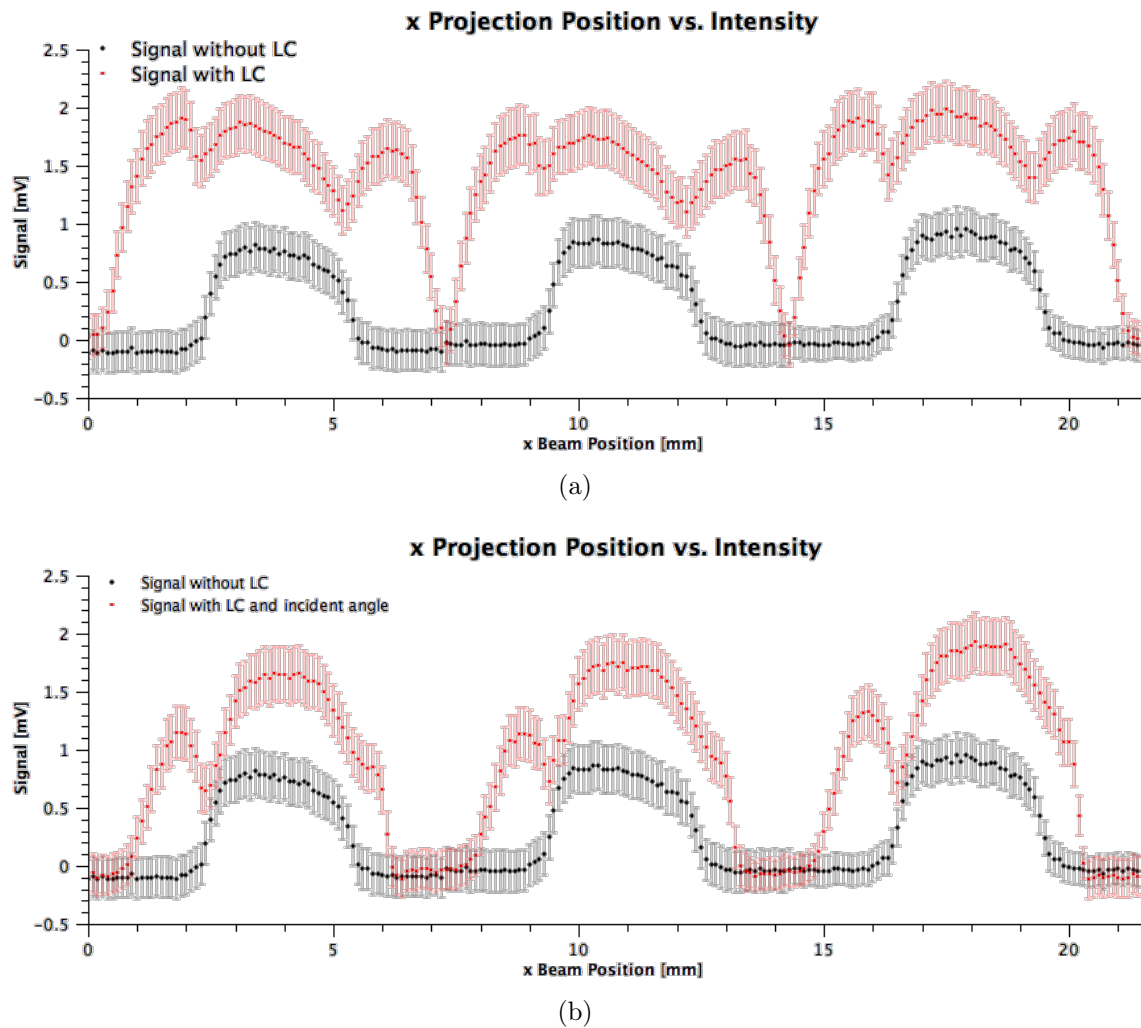
Figure 5.8.: Histogram projections in x-direction of the scan data without LC and with LC
with a) a beam perpendicular to the sensor surface and b) an incident beam
angle of about 15°. The projections show a higher signal on the sensor itself
when the light concentrator is applied. This can be easily explained by looking
at figure 5.7b: as the active area gets increased, the projection naturally gives
a higher signal for the x-range where the sensor itself is located.

Figure 5.9.: Histogram projections in z-direction of the scan data without LC and with LC with a) a beam perpendicular to the detector surface and b) an incident beam angle of about 15°.

5.4. Collection Efficiency

To calculate the collection efficiency of the light concentrator, it is necessary to compare the data from the scans with light concentrator with the data from the scans without it. The collection efficiency ϵ_{col} of one funnel of the light concentrator is defined by

$$\epsilon_{col} = \frac{n_d}{\alpha * n_{d0}}, \tag{5.3}$$

with n_d being the number of photons detected with light concentrator, n_{d0} the number of detected photons without light concentrator and α an area factor [13]. The area factor α represents the enlargement of the detection area of a SiPM and is in this specific case $(\frac{7}{3})^2 \sim 5.44$. This means that the denominator represents the number of photons detected, if the SiPM detection area $(3 \times 3 \text{ mm}^2)$ were of the size of the light concentrator entrance $(7 \times 7 \text{ mm}^2)$. The collection efficiency ϵ_{col} was calculated, using the data presented in chapter 5.3. As no exact information about the number of photons is given, the signal, which corresponds to a certain photon number, was used to calculate ϵ_{col} for a certain
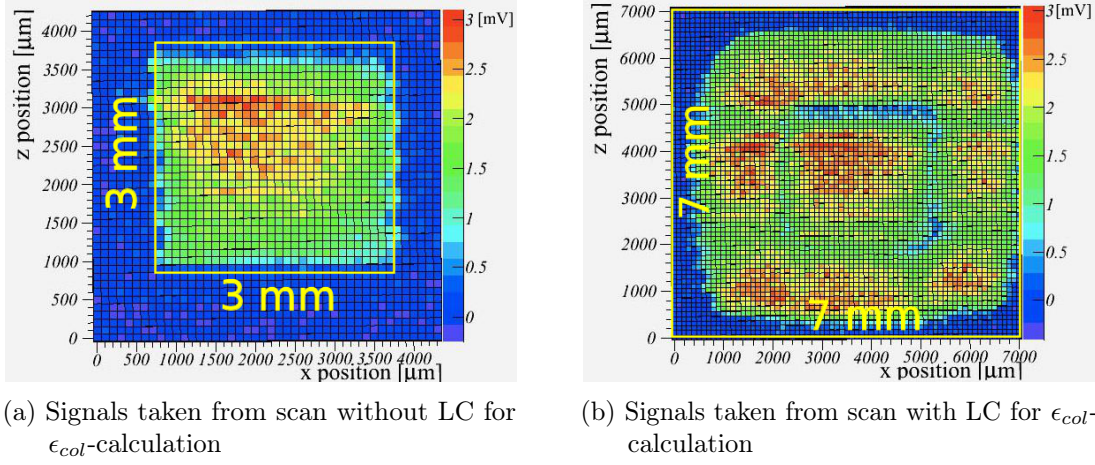
(a) Signals taken from scan without LC for ϵ_{col}-calculation

(b) Signals taken from scan with LC for ϵ_{col}-calculation

Figure 5.10.: Only data within the yellow squares with an area of 3×3 mm^2 and 7×7 mm^2 respectively was taken to calculate the collection efficiency ϵ_{col} of the light concentrator

funnel:

$$\epsilon_{col} = \frac{\Sigma Signal_{LC}}{\Sigma Signal_{noLC} * (\frac{7}{3})^2} \tag{5.4}$$

To achieve an accurate result, the data area of the signal without light concentrator had to be thoroughly chosen. Figure 5.10a illustrates that only data within the yellow square (with an area of 3×3 mm^2) was used to calculate the denominator for ϵ_{col}. Using the best possible estimate for this data range is crucial for achieving an accurate result for the collection efficiency ϵ_{col}. Due to slight variations of the signal intensity from one scan to another, the values from the scans with light concentrator have been normalised to the signal height of the scans without light concentrator.

As the setting of the data range can be chosen arbitrarily for each data set, it has no impact on the ϵ_{col} - calculation that the SiPM was not in centre for the scans without light concentrator (which is the obvious case for the scans shown in figures 5.5a and 5.5c). For the scan with light concentrator, the complete data of a 7×7 mm^2 area was taken (see figure 5.10b).

It was already shown in chapter 5.3, that three different kinds of scans were performed. At first, each of the three channels was scanned separately, first with the light concentrator

on top, then without it. To get a better view of the uniformity of the array, the scan was then performed with all three SiPMs at once. Again, the scans were performed with and without light concentrator. In a third modification, the beam angle was changed by about $15°$ and the three SiPMs with light concentrator were again scanned at once. Table 5.3 shows the mean of the results of the collection efficiency (calculated with formula 5.4) with an incident beam angle of about $0°$ and the results of the collection efficiency for the scan with the beam angle changed by about $15°$. It has to be noted that the result for F4*) only represents the result from the three-sensors scan because the single-sensor scan's data does not reflect the complete funnel, thus giving a significantly lower result. The individual results per scan and channel can be found in appendix B.1.

Table 5.3.: Results of the Collection Efficiency calculation, standard error given in percentage points

Channel	Angle	Collection Efficiency ϵ_{col}	statistical Error
F2	$0°$	88.56 %	0.80 %
F3	$0°$	83.35 %	0.78 %
F4*)	$0°$	86.00 %	1.05 %
F2	$15°$	56.83 %	0.81 %
F3	$15°$	55.41 %	0.75 %
F4	$15°$	58.35 %	0.74 %

6. Discussion

6.1. Uniformity of the light concentrator

Looking at figure 5.7b in chapter 5.3, one can clearly distinguish the active areas from the areas where no photons got detected. Also, it is possible to identify the SiPM sensors themselves, as well as the area of the light concentrator that guided the light onto the SiPMs. There are two main reasons for the areas where no photons got detected: The funnels of the light concentrator are separated by a rim with finite thickness. At these edges incident photons get reflected. Furthermore, the sensors were not soldered onto the sensor board in a perfect alignment, which results in finite gaps between the light concentrator and the sensor on one side and a partial covering of the sensitive area of a sensor on the other side. This leads to undesirable "blind spots" within the active area, which could probably be overcome by improving the alignment of the sensors on the underlying board. Figure 6.1 gives a side-to side view of the two-dimensional histogram and of a photo of the SiPMs and the light concentrator. The photo consists of three photos which were taken with a microscope and merged into one photo. On the photos, taken with a microscope (`Leica MZ8` microscope and `Panasonic GP-KR222` camera) the gaps between the sensitive area of the SiPM, indicated by the visible pixel structure and the light concentrator are obvious. These "blind spots" (or lines in that case) are also reflected in the histogram. In addition, imperfections of the surface of the light concentrator seem to have an influence on the light detection, as is qualitatively indicated by the lower signal at the low right edges of the F2 and F3 SiPMs. The imperfections and gaps are indicated with arrows in figure 6.1.

Another means of inspecting the uniformity of the light concentrator grid is to look at the projections of the two-dimensional histograms in x- and z-direction. The projections in x-direction in figure 5.8a and 5.8b show the cumulated data of the signals with light concentrator in red and the cumulated data of the signals without light concentrator in black. This kind of colour-coding is the same for the z-projections in the figures 5.9a,b.
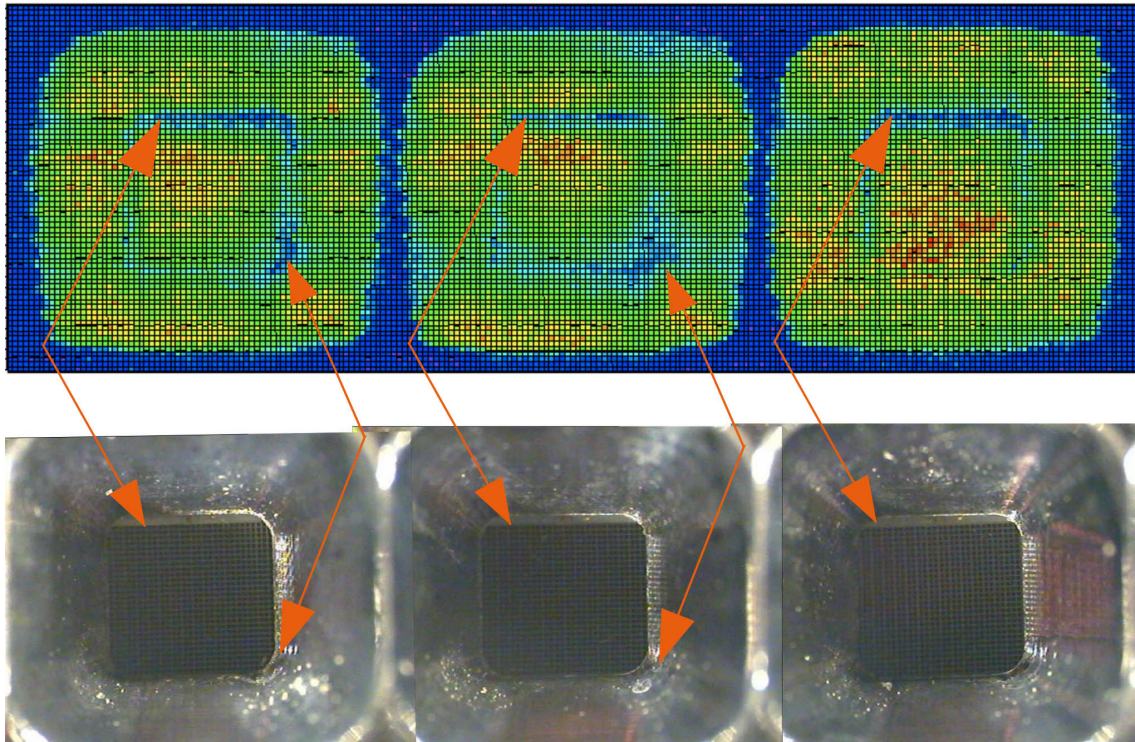
Figure 6.1.: Histogram of signal with light concentrator and photo of light concentrator. The arrows indicate the areas where no or less photons get detected due to imperfections of the SiPM array and the light concentrator.

As has been described in the caption of figure 5.8, the projected signal on the x-axis of the sensor itself is larger with light concentrator than without, due to the increased active area. On the x-projections in figure 5.8a, one can clearly distinguish the region with light concentrator from the region of the SiPM and the brim of the light concentrator. The distribution of the values left and right of the sensor is given by the light concentrator and by the incident beam angle. This can be clearly seen in figure 5.8b, where the variation of the angle of the laser beam significantly reduces the light collection on one side and also reduces the light collection on the other side. The peak left of the SiPM still exists but is much smaller than without an incident beam angle. The peak on the right of the SiPM has vanished, instead there is a sharp edge between the region where no photons get detected and the region where the light concentrator guides some photons onto the sensor.
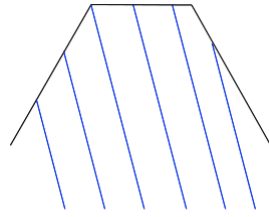
Figure 6.2.: Profile of a light concentrator funnel and incident beam with an angle of about 15°. In a very simplified explanation it can be stated that light only gets reflected onto the sensor area within the range of the topmost left and topmost right blue lines.

Similar explanations can be provided for the projections in z-direction, where the projection is an accumulation of the data for three channels. Again, the distribution of values in figure 5.9a can be interpreted as region with light concentrator for the two maxima on the left and right and as the region of the sensor for the maximum in the centre. In addition, the minima at the beam position of ~ 5 mm for both figures, 5.9a and 5.9b can be explained by the "blind lines" that are caused by the imperfect sensor alignment, as pointed out before and depicted in figure 6.1. The comparability of the projections in x-direction with the projections in z-direction qualitatively imply that the examined funnels of the light concentrator provide a good uniformity, both in form and in coating.

The reduced light guidance for an incident beam with an angle $\neq 0°$ can be descriptively explained, when looking at the drawing in figure 6.2. Changing the beam angle changes the angle at which the light enters and thus the way, the light gets reflected within the light concentrator. This has the effect that light, which enters the light concentrator at a certain point and in a certain angle, can get totally reflected again. With an incident angle, only those photons get reflected onto the sensor, that reach a certain position next to it. This is illustrated in figure 6.2 where only the light within the range of the topmost left and topmost right blue lines gets reflected onto the sensor. This position changes towards the sensor with an increasing incident angle.

6.2. Comparison to simulations of the collection efficiency

The collection efficiency ϵ_{col} of the light concentrator was calculated using equation 5.4 from the data acquired during the scan of the detector module. Simulations of the collection efficiency were done at the institute ahead of construction of the detector module. Figure 6.3 shows the simulated collection efficiency of the light concentrator with a height of 4.5 mm in dependence of the incident beam angle and the quality of the polish [29]. The polish represents the quality of the surface and how much light is reflected/absorbed after reaching the surface.
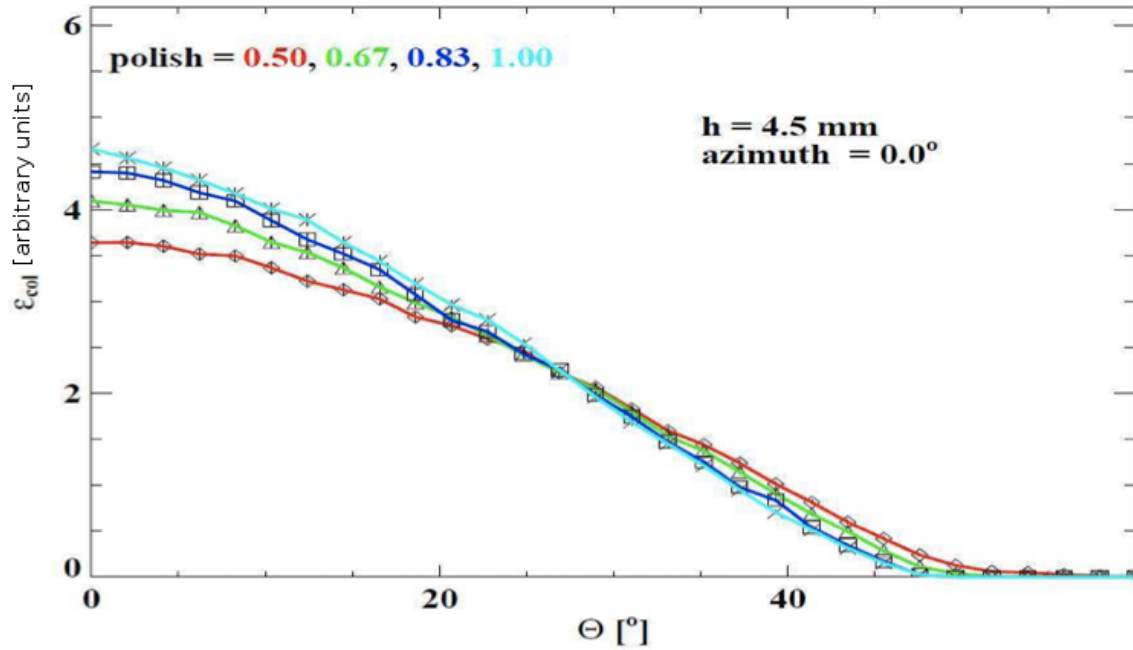
Figure 6.3.: Simulation of the collection efficiency in dependence of the incident beam angle and different surface qualities [29].

The values for the collection efficiency in figure 6.3 is given in regards to the factor $(\frac{7}{3})^2 \sim 5.44$, which is the maximum light collection efficiency (100 %) for a light concentrator with a funnel length of 8 mm. However, for a light concentrator with a height of 4.5 mm, the funnels have a different entrance angle, which reduces the maximum light collection efficiency. This explains why the values of the collection efficiency in figure 6.3 don't reach the maximum value of 5.44.

To compare the results with the simulations, it must be considered, that the simulations assume an entrance area of 7×7 mm^2. However, in reality the light concentrator has rounded edges, as is shown in the figures 5.5 and 5.7. These rounded edges reduce the actual area of a light concentrator funnel. This can be accounted for by multiplying the simulation values by a geometric factor, which in previous work has been defined to be $\epsilon_{geo} = 0.93$ [3]. The simulated value which takes the geometric factor and the reflection coefficient (0.92 for Aluminium at 440nm [30]) into account is about 86 %. The measured values for F2, F3 and F4, which are presented again in table 6.1, are close to this value.

Table 6.1.: Results of the Collection Efficiency calculation, standard errors are presented in table 5.3

Channel	$\boldsymbol{\epsilon_{col}}(0°)$
Simulation	~ 86 %
F2	88.56 %
F3	83.35 %
F4	86.00 %

However, it has to be mentioned that during the scans the wiggle of the x-axis motor, which was already described in section 3.3, could not be completely removed, which can be seen in picture 5.7b, where the boarders on the left and right of each sensor is frayed. This blur of the boarder leads to a slightly lower value for the total signal without light concentrator but has no effect on the total signal for the scans with light concentrator. This means that the measured value for the collection efficiency ϵ_{col} is systematically about 10 % too high. To approximate the influence of the wiggle, the area to calculate the total signal for the scans without light concentrator has been reduced, thus "cutting off" the values that are deemed too low. The approximation for the systematic error is given in appendix B.2.

To compare the measured collection efficiency with the simulated collection efficiency presented in figure 6.3 in dependence of the incident beam angle, the measured values need to be divided by the geometric factor $\epsilon_{geo} = 0.93$, which takes into account that the edges of the light concentrator funnels are round. The new values for ϵ_{col} are presented in table 6.2. The simulated ϵ_{col} value for an incident beam angle of about 15° for an aluminium coated funnel with a height of 4.5 mm is about 61 %. The measured values lie

Table 6.2.: Results of the measured collection efficiency for an incident beam angle of 15°
and results comparable to the simulation.

Channel	$\boldsymbol{\epsilon_{col}(15°)}$	$\boldsymbol{\epsilon_{col}(15°)/\epsilon_{geo}}$
Simulation	−	$\sim 61\ \%$
F2	56.83 %	61.11 %
F3	55.41 %	59.58 %
F4	58.35 %	62.74 %

within the simulations, but it has to be noted again, that the measured values are about 10 % too high.

In addition to the fact that the measured values are close to the simulated values for the collection efficiency ϵ_{col}, the variance of the measured values for ϵ_{col} for the scanned funnels implies that the examined funnels of the light concentrator provide a good uniformity within $4\% - 5\%$.

7. Summary and Conclusion

In this work, a prototype SiPM Cherenkov light detector module was scanned to test the uniformity of the array and to measure the collection efficiency ϵ_{col} of the light concentrator that was specifically designed for this position sensitive detector. For the scans with a stepping size of $100\ \mu$m, a special setup in regards to the beam spot size and beam path as well as the movement of the beam was produced. To conduct the experiment efficiently, an automation routine was written. This routine moved the beam spot position on the detector in two dimensions by controlling two stepping-motors. In addition, the program established communication with the oscilloscope that was used to acquire the signals and saved the data on the computer into a text file.

Scans of the SiPM array were performed for three randomly chosen adjacent sensors with and without light concentrator on top. The performance of the light concentrator collection efficiency was tested for two different incident light beam angles, $\sim 0°$ and $\sim 15°$.

The data of the scans provided in chapter 5.3 give a good picture of the uniformity of the scanned light concentrator array. The projected data behaves similarly in x-direction and in z-direction, proving that the scanned funnels provide a good uniformity.

The measured collection efficiency ϵ_{col} is in good agreement with the simulations, both, for an incident beam angle of $0°$ (on average $85.97\ \% \pm 0.51\ \%$ measured vs. $\sim 86\ \%$ simulation) and $15°$ (on average $56.86 \pm 0.44\ \%$ measured vs. $\sim 61\ \%$ simulation) . In addition, the small variance between the measured values for the collection efficiency of the three funnels leads to the conclusion, that the scanned funnels provide a good uniformity within $4 - 5\%$.

List of Abbrevations

APD	Avalanche Photo Diode
DIRC	Detection of Internally Reflected Cherenkov Light
FAIR	Facility for Antiproton and Ion Research
FWHM	Full Width Half Maximum
LC	Light Concentrator
LED	Light Emitting Diode
MPPC	Multi-Pixel Photon Counter (Hamamatsu SiPM)
PANDA	anti-Proton ANnihilation at DArmstadt
PDE	Particle Detection Efficiency
PMT	Photomultiplier Tube
SiPM	Silicon Photomultiplier
SPAD	Single-Photon Avalanche Diode
VI	Virtual Interface

A. LabView Sub VIs

The main LabView VI used in the experiment, "**_MercuryMotorOszi.vi**" consists of many sub VIs that contain certain commands. They are used for better overview of the main VI. This appendix describes the sub VIs used, their main function and the parameters that influence the data acquisition and function of the program. In figure A.1 one can see the hierarchy tree of the described sub VIs. Note that this figure is a simplified version of the complete hierarchy tree which wouldn't fit on one page.
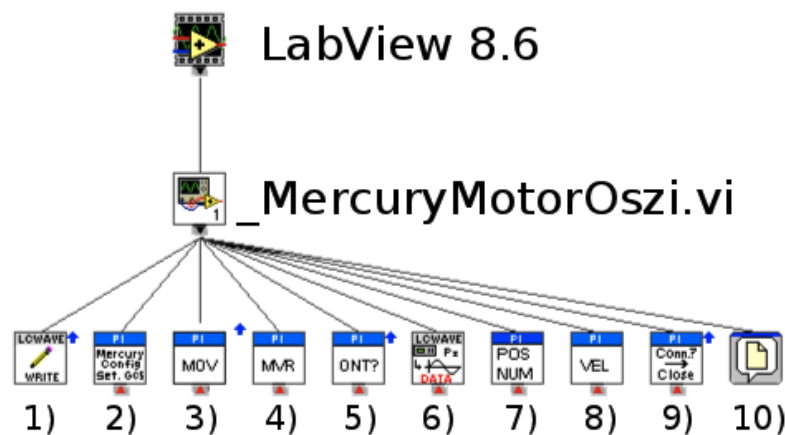
Figure A.1.: LabView hierarchy of the used sub VIs. 1) LeCroy Wave Series.lvlib:Write.vi, described in subsection A.2.2, 2) Mercury_GCS_Configuration_Setup.vi, described in subsection A.1.1, 3) MOV.vi, described in subsection A.1.4, 4) MVR.vi, described in subsection A.1.7, 5) ONT?.vi, described in subsection A.1.5, 6) OsziData.vi, described in subsection A.2.1, 7) POS_Num.vi, described in subsection A.1.6, 8) VEL.vi, described in subsection A.1.3, 9) Close connection if open.vi, described in subsection A.1.2 and 10) File Dialog, a LabView native VI that got mentioned in chapter 4.1.

A.1. Virtual Interfaces for the actuators, provided by the manufacturer (PI)

A.1.1. Mercury_GCS_Configuration_Setup.vi

This sub VI performs all necessary tasks to successfully connect the actuator and the respective controller to the PC. This VI cannot be altered as it was password protected by the manufacturer. With this VI one can define the type of connection (USB, USB Daisy Chain, RS-232, etc.), the main and the other controllers, and whether or not to look for controllers. After connecting the controllers and actuators, the stepping motors start moving towards a reference point, which is set at 12.5 mm. When the setup is completed, one can read the identification of the controllers, the number of connected axes, the position of the respective system and the moving range in the mask "Mercury Controller Setup" of the main VI.

A.1.2. Close connection if open.vi

The VI closes the connection between the actuator controllers and the PC. It is necessary to properly close the connection, otherwise communication errors occur that can only be resolved by a shutdown of the controllers and a restart of LabView. This VI is the last one used in the "_MercuryMotorOszi.vi" program.

A.1.3. VEL.vi

With this VI one can set the velocity of the motor movement. The actuator rod's basic velocity is 0.75 mm/s. For the experiment the velocity was set to 1.0 mm/s for both actuators.

A.1.4. MOV.vi

This VI sets the actuator tip to an absolute position. This sub VI was used to set the two axes to an origin. In the case of the experiment the origin was generally put at 1 mm each, however one could set the origin at any other point too.

A.1.5. ONT?.vi

ONT? asks if the actuator is already set on target and gives a boolean as answer.

A.1.6. POS_Num.vi

The VI is a modification of the VI 'POS?.vi" which asks for the current position of the actuator tip and returns the information as a double. The actuator's minimal stepping size is 1 μm but the actuator returns digits that would imply an even better precision. However, only the first three digits after the comma are significant, the others don't give useful information. To get the correct μm number, one has to round the 4th digit after the comma. To do this automatically, the VI "POS_NUM" was written. It acquires the information about the position and then changes the number into an exponential with only 2 significant digits. This means that the LabView precision of the motors gets limited to 10 μm instead of 1 μm. The number is then transformed back into a double with the digits 4 to 6 after the comma being zeros. That transformed number is written into the text-file. It is important to first make sure that the motor is on position before asking for the position. This is due to the fact that the motor can send back the position while it is still moving. However, for data acquisition we need the position after completing the move. To make sure that data wasn't recorded before the move was complete, the *ONT?.vi* was used in advance of any data acquisition.

A.1.7. MVR.vi

MVR is used to move the actuator tips by a certain distance. The VI is used to change the position of the actuators by the value "stepping size" which set on the front panel of the main VI.

A.2. Virtual Interfaces for the oscilloscope, provided by the manufacturer

A.2.1. OsziData.vi

The VI is based upon the Acquire and Read MyMeasurements.vi. This VI is provided by LeCroy. One has to define the communication standard and set the IP address of the oscilloscope. Next, one has to define the parameter number, that one wants to read out. As we can read out three channels simultaniously (the 4th channel being used for the trigger input), we set the parameters to P1, P2 and P3 respectively. The VI then returns data values, such as minimum, maximum, current value, sigma, mean and number

of samples. Having set the MyMeasurement of the oscilloscope to the minimum of the respective channel, we only take the mean and sigma of the minimum. This information is written into the text-file for each channel and position.

A.2.2. LeCroy Wave Series.lvlib:Write.vi

This VI clears the samples and recorded data on the oscilloscope itself after the data had been sent to the computer and saved in the text file. Calling this routine ensures that only the mean for a current coordinate gets calculated and submitted.

A.3. Write To Spreadsheet File (DBL)_custom.vi

The VI that is part of the original LabView VI set was changed. The connectors got different and an error in, error out option was added. This error option is important as it guaranteed that the next step would not start before saving the data in the text file was completed.

B. Collection Efficiency Table

B.1. Measured collection efficiency

The collection efficiency for each of the channels F2, F3 and F4 for each scan is provided here. The performed scans were: F2, F3, F4 each with and without light concentrator as well as one scan of all three sensors at once, again with and without light concentrator. In addition, a scan for all sensors at once was performed with an incident beam angle of $\sim 15°$.

Table B.1.: Results of the Collection Efficiency calculation, standard error given in percentage points

Channel and Method	Collection Efficiency ϵ_{col}	statistical Error
F2 Single Sensor Scan	88.874 %	1.115 %
F3 Single Sensor Scan	82.764 %	1.075 %
F4 Single Sensor Scan	78.083 %	0.891 %
F2 Three Sensor Scan	88.254 %	1.158 %
F3 Three Sensor Scan	83.934 %	1.124 %
F4 Three Sensor Scan	86.007 %	1.049 %
F2 Angle Scan	56.829 %	0.806 %
F3 Angle Scan	55.408 %	0.753 %
F4 Angle Scan	58.352 %	0.737 %

B.2. Measured collection efficiency with different approach

As is mentioned in chapter 6.2, the measured values for the total signal without light concentrator is slightly too low because of a wiggle of the motor. To estimate the effect of the lower signal, the calculation of the total and of the collection efficiency has been changed

in the following way: The range of data for the total signal without light concentrator has been changed from 3×3 mm^2 to 2.8×2.8 mm^2. This leads to "cutting off" the values that are potentially too low because of the "geographic offset". The formula then had to be changed into

$$\epsilon_{col} = \frac{\Sigma Signal_{LC}}{\Sigma Signal_{noLC} * (\frac{7}{2.8})^2}, \tag{B.1}$$

because the active area of the SiPM had been artificially changed. The new values are presented in table B.2. Comparing these new values with the collection efficiency values that include the wiggle implies that the measured values are about 10 % too high.

Table B.2.: Results of the Collection Efficiency calculation, standard error given in percentage points

Channel and Method	Collection Efficiency ϵ_{col}	statistical Error
F2 Single Sensor Scan	80.207 %	1.151 %
F3 Single Sensor Scan	75.165 %	1.118 %
F4 Single Sensor Scan	71.291 %	0.932 %
F2 Three Sensor Scan	80.859 %	1.219 %
F3 Three Sensor Scan	76.610 %	1.178 %
F4 Three Sensor Scan	80.270 %	1.131 %
F2 Angle Scan	52.069 %	0.848 %
F3 Angle Scan	50.590 %	0.789 %
F4 Angle Scan	54.456 %	0.794 %

List of Figures

Bibliography

[1] D. H. Perkins. *Introduction to High Energy Physics*. Cambridge University Press, 4th edition, 2000.

[2] F. Powolny. *Characterization of time resolved photodetector systems for Positron Emission Tomography*. PhD thesis, Université de Neuchatel, 2009.

[3] L. Gruber, G. Ahmed, S. Brunner, P. Bühler, J. Marton, and K. Suzuki. Position sensitive SiPM detector for Cherenkov applications. *Journal of Instrumentation*, 6:C11024, 2011.

[4] J.L. Moll. *Physics of semiconductors*. McGraw-Hill, 1964.

[5] S.M. Sze. *Semiconductor devices, physics and technology*. Wiley, 1985.

[6] C. Kittel. *Introduction to solid state physics*. Wiley, 7th edition, 1996.

[7] J. Singh. *Semiconductor devices: basic principles*. Wiley, 2011.

[8] S. Vasile, P. Gothoskar, R. Farrell, and D. Sdrulla. Photon detection with high gain avalanche photodiode arrays. *IEEE Transactions on Nuclear Science*, 45:720–723, 1998.

[9] H. Dautet, P. Deschamps, B. Dion, A. D. MacGregor, D. MacSween, R. J. McIntyre, C. Trottier, and P. P. Webb. Photon counting techniques with silicon avalanche photodiodes. *Applied Optics*, 32:3894–3900, 1993.

[10] S. Cova, M. Ghioni, A. Lacaita, C. Samori, and F. Zappa. Avalanche photodiodes and quenching circuits for single-photon detection. *Applied Optics*, 35:1956–1976, 1996.

[11] D. Renker. Geiger-mode avalanche photodiodes, history, properties and problems. *Nuclear Instruments and Methods in Physics Research*, A567:48–56, 2006.

[12] Hamamatsu. Opto-Semiconductor Handbook, p. 52, 2010.

[13] G. Ahmed. *Development of sensitive detectors for subatomic physics experiments*. PhD thesis, Al-Azhar University, Cairo, 2011.

[14] V. Golovin and V. Saveliev. Novel type of avalanche photodetector with Geiger mode operation. *Nuclear Instruments and Methods in Physics Research*, 518:560 – 564, 2004.

[15] J.C. Jackson, D. Phelan, A.P. Morrison, R.M. Redfern, and A. Mathewson. Characterization of Geiger Mode Avalanche Photodiodes for Fluorescence Decay Measurements. *SPIE Proceedings Photodetector Materials and Devices VII*, 4650-7, 2002.

[16] C. Piemonte. A new Silicon Photomultiplier structure for blue light detection. *Nuclear Instruments and Methods in Physics Research*, 568:224 – 232, 2006.

[17] P. Buzhan, B. Dolgoshein, L. Filatov, A. Ilyin, V. Kantzerov, V. Kaplin, A. Karakash, F. Kayumov, S. Klemin, E. Popova, and S. Smirnov. Silicon photomultiplier and its possible applications. *Nuclear Instruments and Methods in Physics Research*, 504:48 – 52, 2003.

[18] S. Cova, M. Ghioni, A. Lotito, I. Rech, and F. Zappa. Evolution and prospects for single-photon avalanche diodes and quenching circuits. *Journal of Modern Optics*, 51:1267–1288, 2004.

[19] W. Leo. *Techniques for Nuclear and Particle Physics Experiments*, volume 2. Springer, 1994.

[20] Panda Collaboration. Letter of intent for PANDA, http://www-panda.gsi.de/archive/public/panda_loi.pdf, 2004.

[21] J. Schwiening. The Barrel DIRC for the PANDA EXPERIMENT at FAIR. In *http://www-win.gsi.de/r3b/HIC4FAIR_ Talks/Schwiening_ HICforFAIR_ Feb2011.pdf*, 2011.

[22] C. Schwarz, G. Ahmed, A. Britting, P. Bühler, E. Cowie, V.Kh. Dodokhov, M. Düren, D. Dutta, W. Eyrich, K. Föhl, D.I. Glazier, A. Hayrapetyan, M. Hoek, R. Hohler, A. Lehmann, D. Lehmann, R. Kaiser, T. Keri, P. Koch, B. Kröck, J. Marton, O. Merle, R. Montgomery, K. Peters, S. Reinicke, G. Rosner, B. Roy, G. Schepers, L. Schmitt,

J. Schwiening, B. Seitz, C. Sfienti, K. Suzuki, F. Uhlig, A.S. Vodopianov, D.P. Watts, and W. Yu. Particle identification for the detector. *Nuclear Instruments and Methods in Physics Research*, 639:169 – 172, 2011.

[23] C. Schwarz et al. The Barrel DIRC of PANDA. *Journal of Instrumentation*, 7, 2012.

[24] Hamamatsu. Datasheet S10931-100P, http://sales.hamamatsu.com/assets/pdf/parts_S /s10362-33series_kapd1023e05.pdf, 2009.

[25] S. Korpar, H. Chagani, R. Dolenec, K. Hara, T. Iijima, P. Križan, Y. Mazuka, R. Pestotnik, A. Stanovnik, and M. Yamaoka. Measurement of Cherenkov photons by SiPMs with light guides. *Nuclear Instruments and Methods in Physics Research*, 610:427 – 430, 2009.

[26] Physikinstrumente. Mp86e User Manual M-228 and M-229 Stepper-Mike Linear Actuators 1.1.0. www.pi.ws, 2009.

[27] Gaussian Beams and the Knife-Edge Measurement, http://massey.dur.ac.uk/resources/grad_skills/knifeedge.pdf.

[28] ROOT Version 5.28/00. http://root.cern.ch/drupal/, 1995-2012.

[29] G. Ahmed, P. Bühler, M. Cargnelli, R. Hohler, J. Marton, H. Orth, and K. Suzuki. Application of Geiger-mode photosensors in Cherenkov detectors. *Nuclear Instruments and Methods in Physics Research*, 639:107 – 110, 2011.
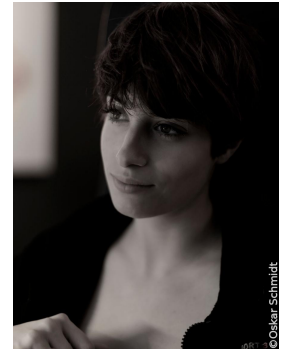
[30] Refractive Index Database. http://refractiveindex.info.

Acknowledgement

Curriculum Vitae

Mariana Rihl

Born:	November 13, 1986
	in Vienna, Austria
Nationality:	Austrian

Education and Work Experience

12/2011-11/2012	Diploma student in Detector Physics
	Stefan Meyer Institute of the Austrian Academy of Sciences
7/2011	Internship at ASACUSA Experiment at CERN
	Stefan Meyer Institute of the Austrian Academy of Sciences
05/2008-12/2011	Business Analyst (part-time)
	Microsoft Austria GmBH
09/2007-02/2008	Internship
	Deloitte Austria
07/2007	Internship
	SAP Austria GmBH
09/2006-12/2006	Participation in Erasmus programme
	ESC Dijon, France

07-08/2006	Internship
	SAP Austria GmBH
07-08/2005	Internship
	Baxter AG Austria
since 10/2005	Undergraduate studies in physics (equivalent to M.Sc.)
	University of Vienna
09/2004-06/2008	Diploma studies "European economy and management"
	graduation with Mag.(FH) diploma
	Fachhochschule des bfi Vienna
06/2004	High school graduation with merit
	Musikgymnasium Vienna

Languages

German	native
English	fluently written and spoken
French	fluently written and spoken
Spanish	basic skills

Computer Skills

Programming	C, ROOT, LabView
Scientific Editing	LaTeX , QTIPlot, Origin
Graphical Editing	Inkscape, Photoshop
Others	Office applications
Operating Systems	Mac OS, Win OS, Linux

Conference Proceedings

Industry-academia matching event on SiPM and related technologies: "Improving Time of Flight PET using Silicon Photomultipliers", S.E. Brunner, L.Gruber, A. Hirtl, M. Jankovec, P. Knoll, J. Marton, M. Rihl, K. Suzuki